Optical remote sensing of planetary atmospheres

Observation methods

Merits and demerits

	Lander	Orbiter	Ground-based observation
Spatial coverage	Limited	Global	Global
Time coverage	Short in many cases	Long & continuous	Repeatable
Observable variables	- In-situ measurements - Many options	- Optical/radio remote sensing - In-situ plasma measurements	- Optical/radio remote sensing - Instruments can be large

Recent/future remote sensing (orbiter) missions

Venus Express

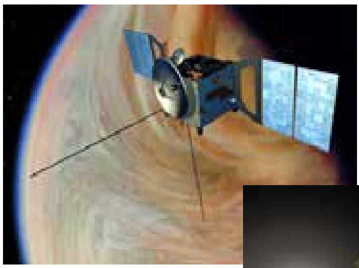

Akatsuki

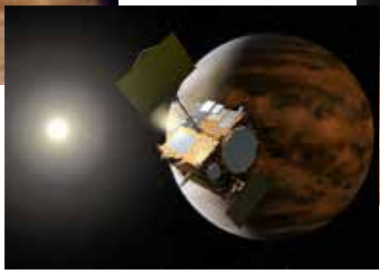

Mars Reconnaissance Orbiter

JUNO

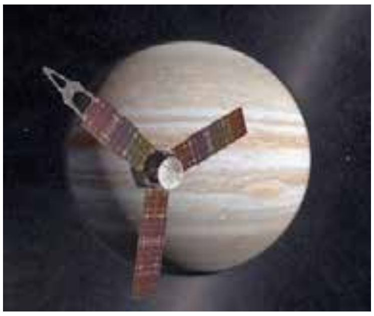

ExoMars Trace Gas Orbiter

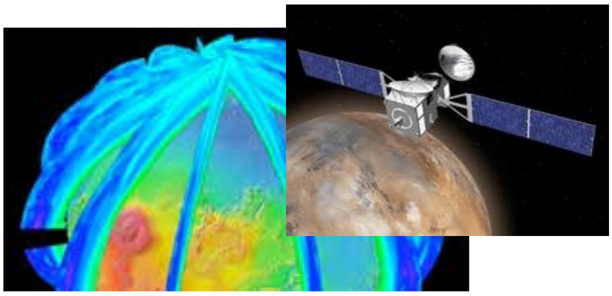

MMX

JUICE

Interaction between molecules and electromagnetic waves

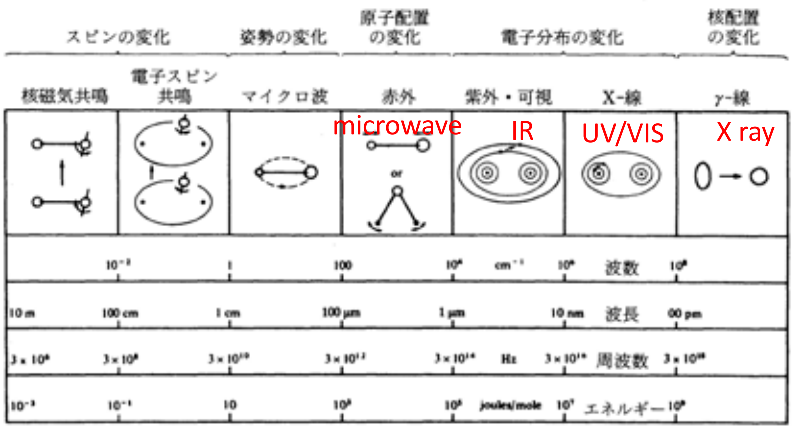

図 5.1 電磁波のスペクトルと電磁波–分子 (原子) の相互作用のメカニズム (Banwell and McCash, 1994)[26)]

柴田（1999）

Andrews (2010)

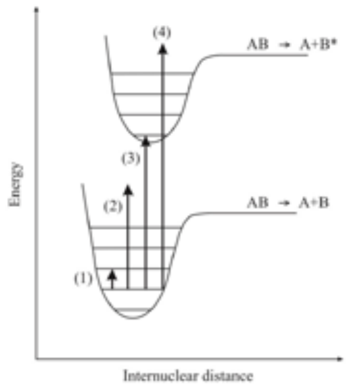

Schematic energy diagram for a diatomic molecule. See text for details.

Remote sensing of atmospheres

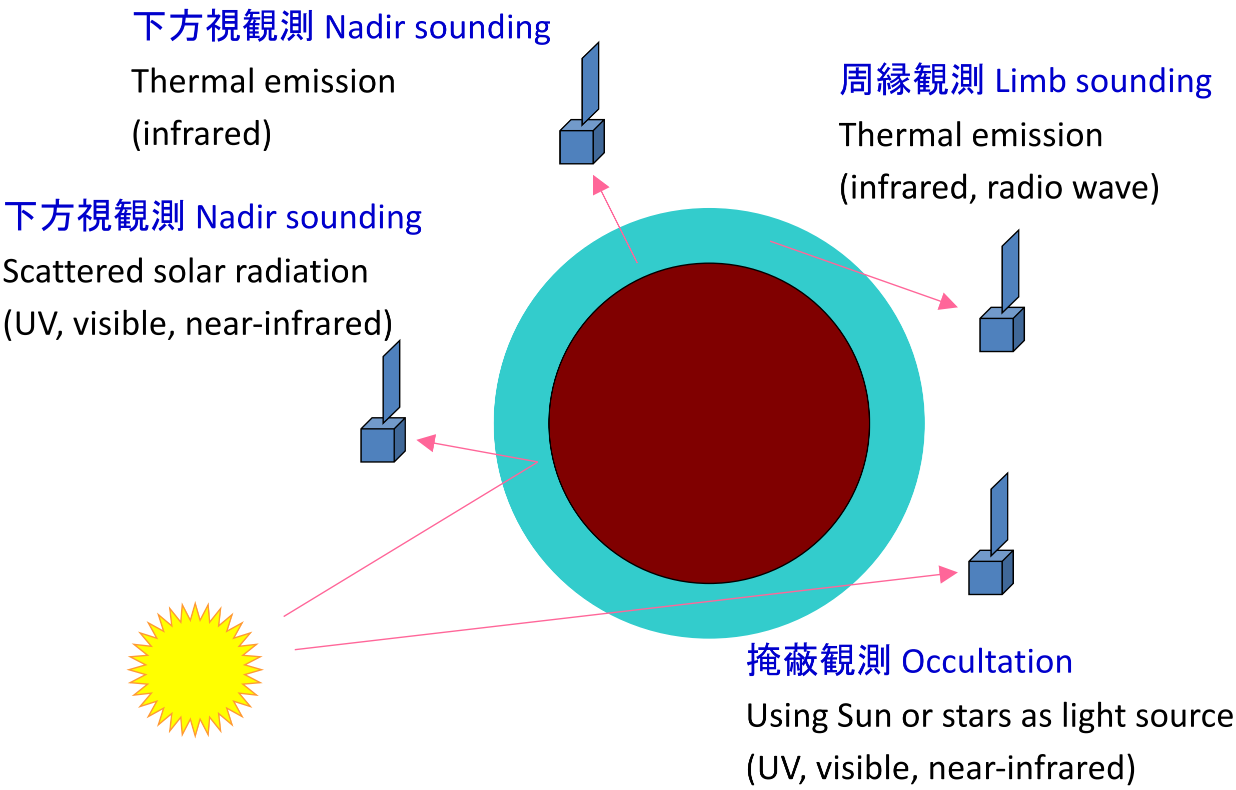

Imaging

Himawari (meteorological satellite) imaging channels

JMA Himawari HP

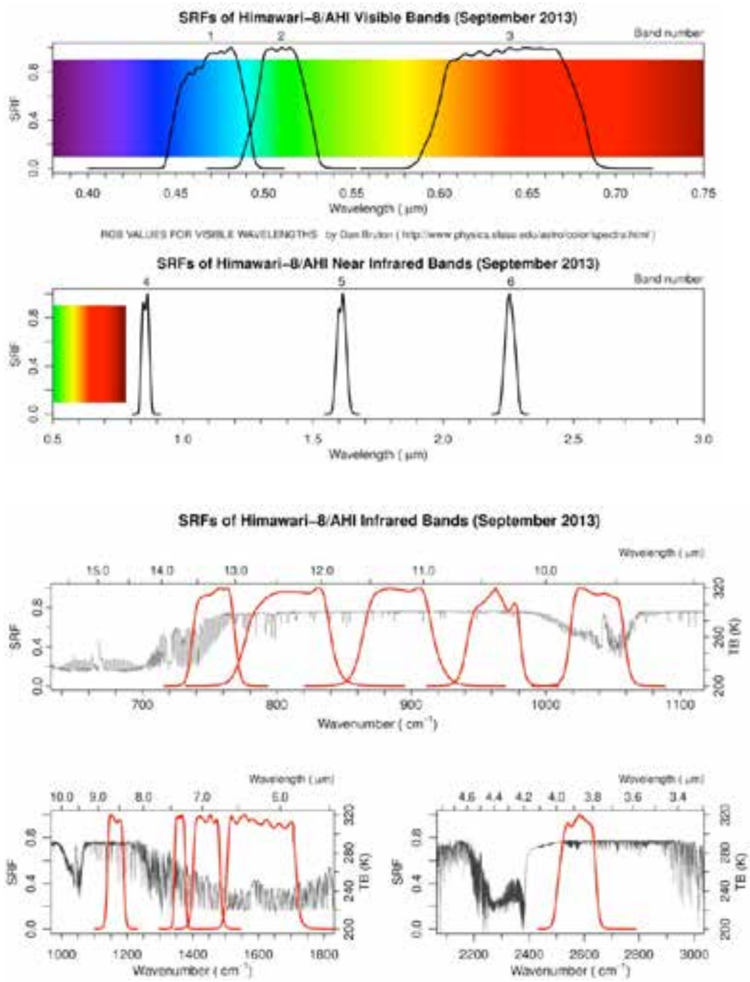

Interference filter

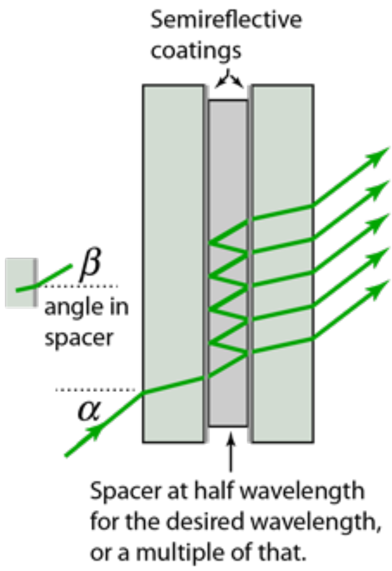

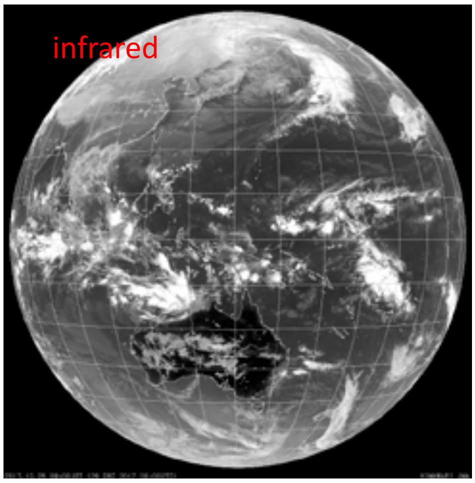

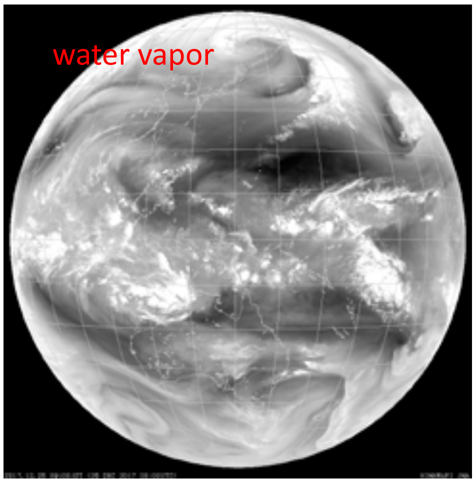

Junocam: Juno's Outreach Camera

Hansen et al. (2014)

Fig. 12 Color filters are bonded directly to the CCD

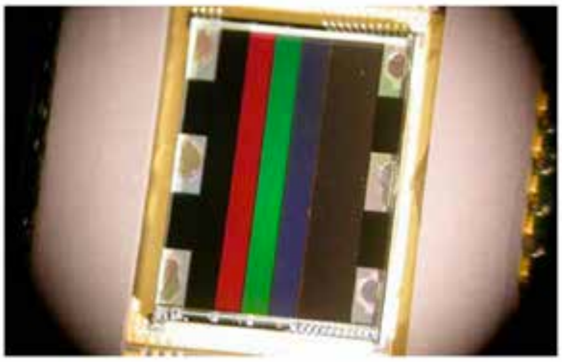

Table 3 Junocam filter characteristics

Band	Blue	Green	Red	Methane
Center wavelength	480.1 nm	553.5 nm	698.9 nm	893.3 nm
FWHM	45.5 nm	79.3 nm	175.4 nm	22.7 nm

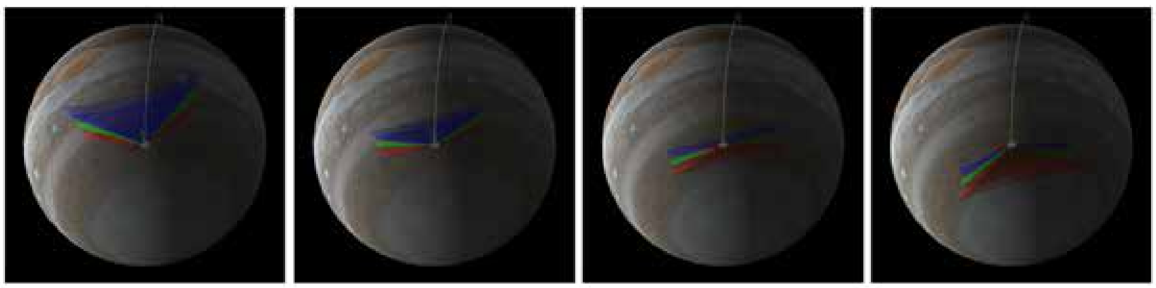

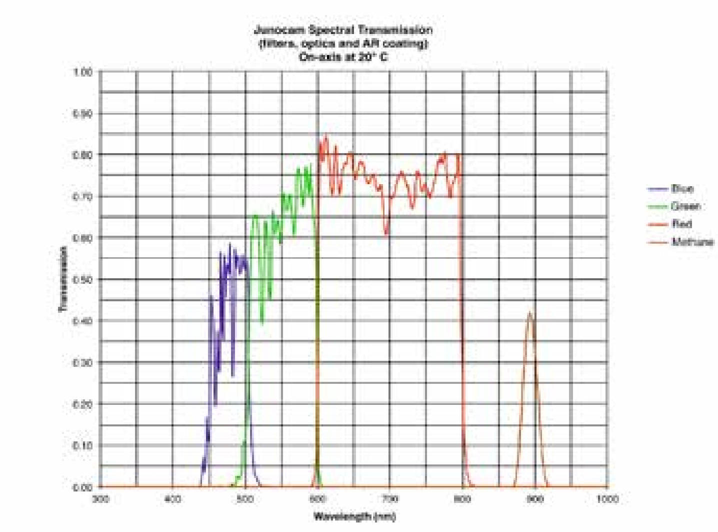

Fig. 13 Bandpasses and transmission are shown for Junocam's four filters

Onboard instruments

Instrument	FOV	Detector	Filters	Width	Targets
1-μm Camera **IR1**	12°	Si-CSD/CCD 1024 x 1024 pix	1.01 μm (night)	0.04 μm	Surface, Clouds
			0.97 μm (night)	0.04 μm	H_2O vapor
			0.90 μm (night)	0.03 μm	Surface, Clouds
			0.90 μm (day)	0.01 μm	Clouds
2-μm Camera **IR2**	12°	PtSi-CSD/CCD 1024 x 1024 pix	1.735 μm (night)	0.04 μm	Clouds, Particle size
			2.26 μm (night)	0.06 μm	
			2.32 μm (night)	0.04 μm	CO below clouds
			2.02 μm (day)	0.04 μm	Cloud-top height
			1.65 μm (cruise)	0.3 μm	Zodiacal light
UltraViolet Imager **UVI**	12°	Si-CCD 1024 x 1024 pix	283 nm (day)	15 nm	SO_2 at cloud top
			365 nm (day)	15 nm	Unknown absorber
Longwave IR Camera **LIR**	12.4X 16.4 °	Bolometer 248 x 328 pix	10 μm (day/night)	4 μm	Cloud-top temperature
Lightning & Airglow Camera **LAC**	16°	8 x 8 APD (50kHz sampling in lightning mode)	777.4 nm (night)	4.2 nm	OI lightning
			552.5 nm (night)	4.7 nm	O_2 HerzbergII ariglow
			557.7 nm (night)	3.1 nm	OI airglow
			630.0 nm (night)	3.5 nm	OI airglow
Ultra-stable oscillator for Radio Science **RS**			X-band (8.4GHz)		Vertical prifiles of T, H_2SO_4 (g), Ne

Venus seen by Akatsuki

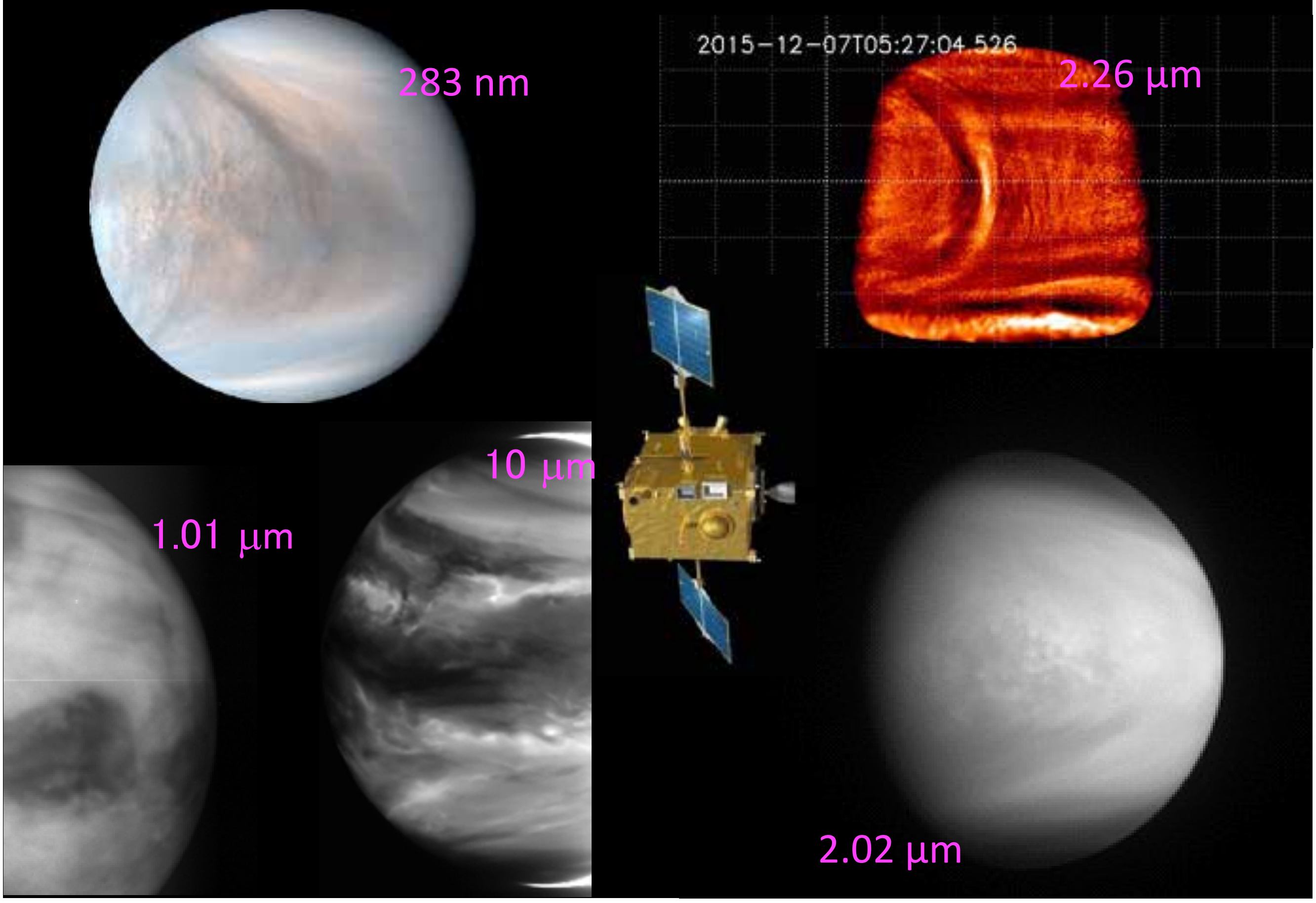

Spectroscopy

Absorption lines

Extinction coefficient

line-shape function

$$k_\nu = \sum_n S_n f_n(\nu - \nu_n)$$

line strength

Andrews (2010)

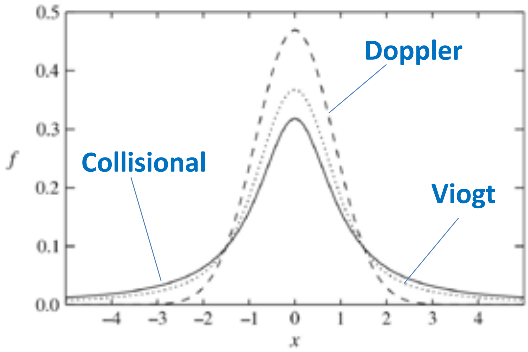

Illustrating the Lorentz (solid), Doppler (dashed) and Voigt (dotted) line shapes as a function of $x = (\nu - \nu_0)/\alpha$, where α is the half-width at half maximum appropriate for each shape. The curves are normalised such that the area under each is the same.

Collisional broadening

$$f(\nu - \nu_n) = \left(\frac{\gamma_L}{\pi}\right) \frac{1}{(\nu - \nu_n)^2 + \gamma_L^2}$$

$$\gamma_L \propto p\, T^{-1/2}$$

Dominant in the lower atmosphere

Doppler broadening

$$k_\nu = \frac{S}{\gamma_D \sqrt{\pi}} \exp\left(-\frac{(\nu - \nu_0)^2}{\gamma_D^2}\right)$$

$$\gamma_D = \frac{\nu_0}{c} \left(\frac{2 k_B T}{m}\right)^{1/2}$$

Dominant in the upper atmosphere

Grating spectrometer

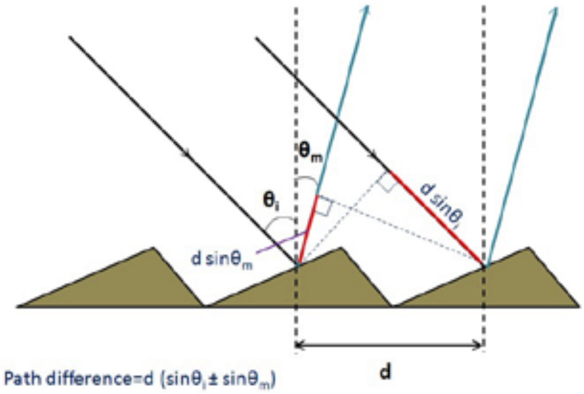

From Wikipedia

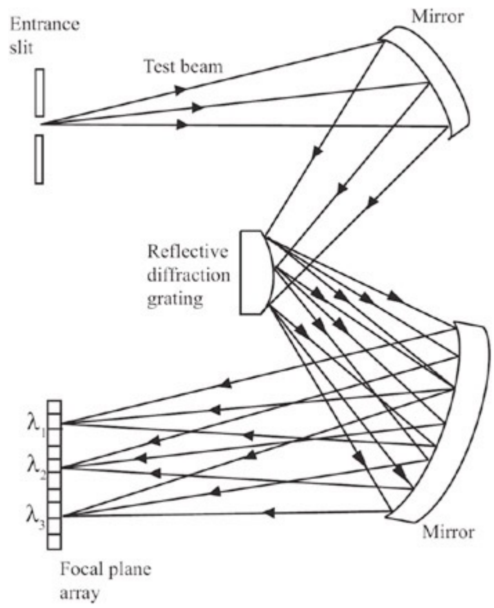

Crawford (2007)

Fourier spectrometer

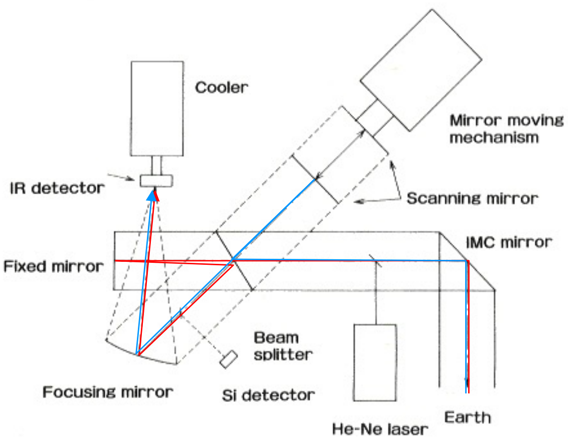

ADEOS/IMG Optical System

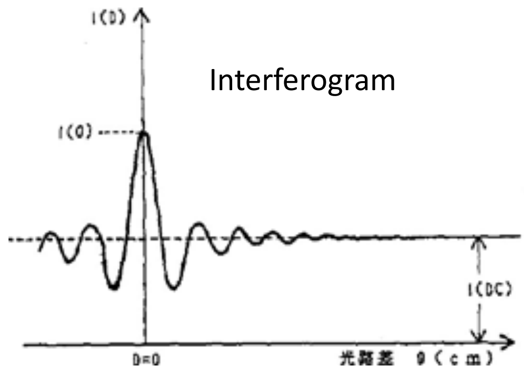

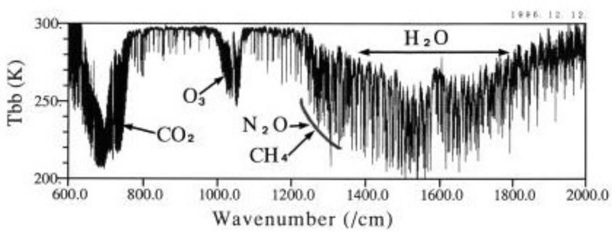

Interferogram →(FFT)→ Spectrum

GOSAT
Fourier Transform
Spectrometer

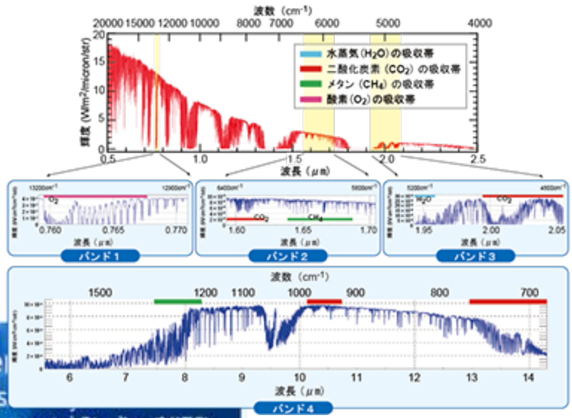

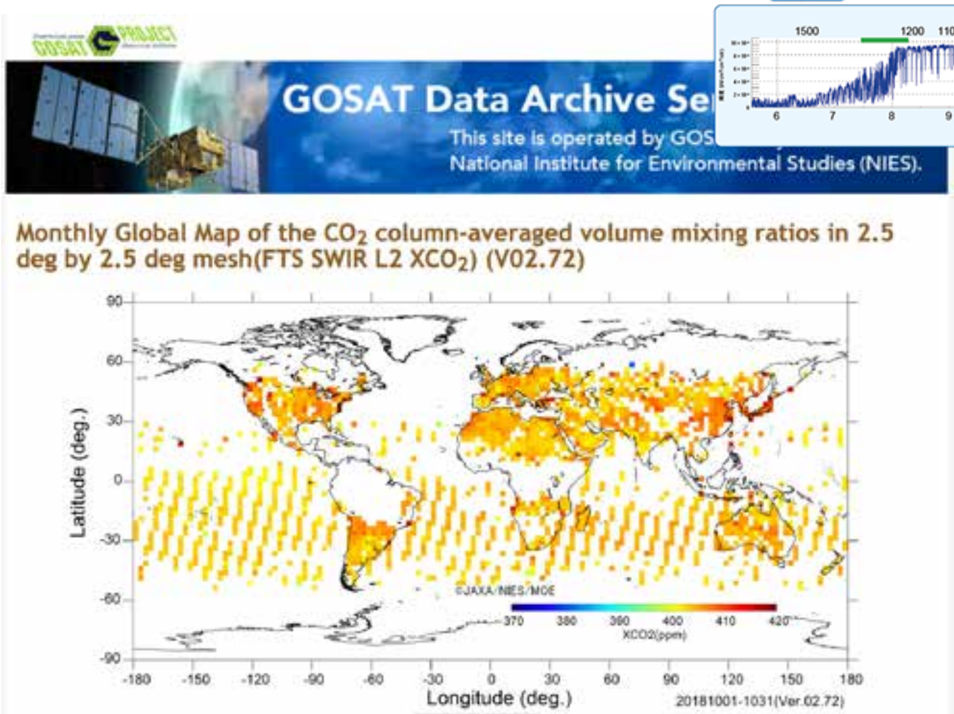

Retrieval of vertical structures from nadir-looking infrared spectra

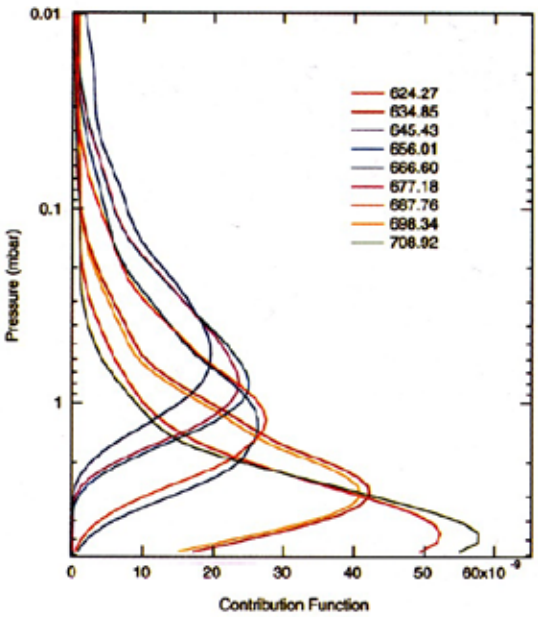

Contribution functions for wavelengths in CO_2 15 μm band for Mars atmosphere

(Conrath et al. 2000)

Outgoing radiance:

$$I = B(T_S)\exp(-\tau_s) + \int_0^{\tau_s} B(T(\tau))\exp(-\tau)\,d\tau$$

$$= B(T_s)\exp(-\tau_s) + \int_0^{\infty} B(T(z))\,\underline{k_a(z)\exp(-\tau(z))}\,dz$$

Optical thickness

$$\tau = \int_z^{\infty} k_a\,dz$$

I：radiance(J/m2/s/str/Hz)
B：Planck function
k_a：absorption coefficient
z：altitude

Thermal emission spectra of Mars

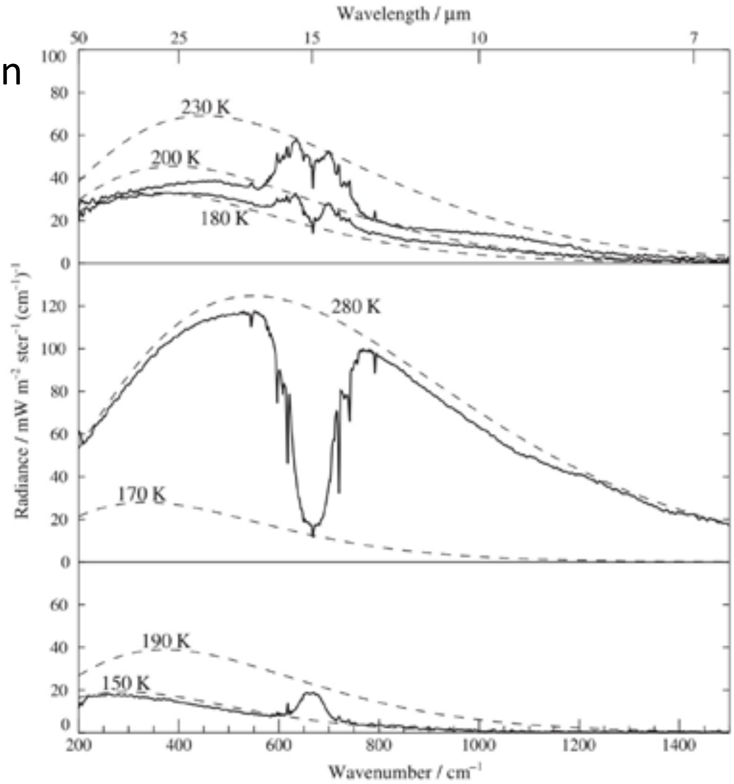

Andrews (2010)

Emission spectra from Mars obtained with the IRIS instrument on Mariner 9 (adapted from Hanel *et al.* (1972)). Top panel: spectra recorded over the south polar region; upper curve includes a smaller fraction of the polar ice cap than the lower curve. Middle panel: spectrum recorded near 21° S. Lower panel: spectrum recorded near 66° N; note that the condensation temperature of CO_2 at Martian surface pressures is about 145 K. Diagram prepared with the help of Dr S. R. Lewis, using data from the Planetary Data System.

Temperature retrieval from infrared spectra taken by Mars Global Surveyor/TES

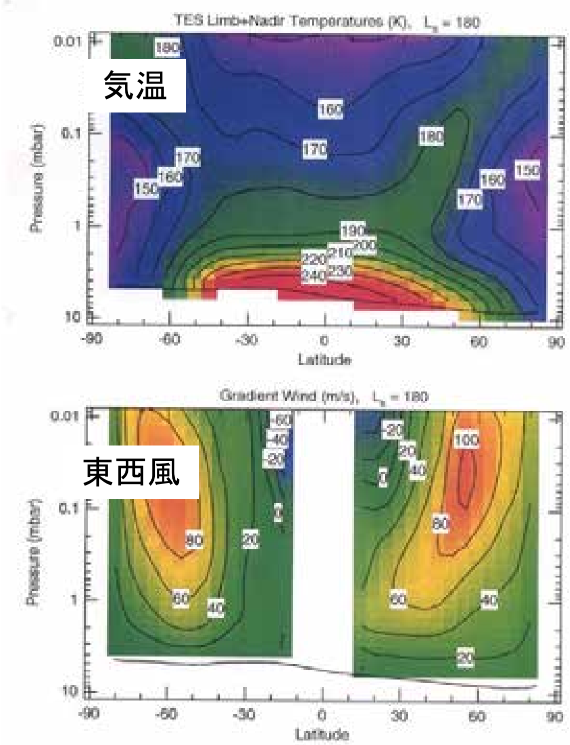

Smith et al. (2001)

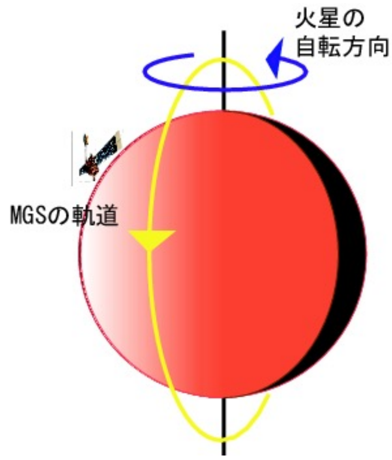

温度風：$$\frac{\partial u_g}{\partial p} = \frac{R}{fp}\frac{\partial T}{\partial y}$$

Retrieval of the atmospheric composition of Venus from infrared spectra taken by ground-based telescopes

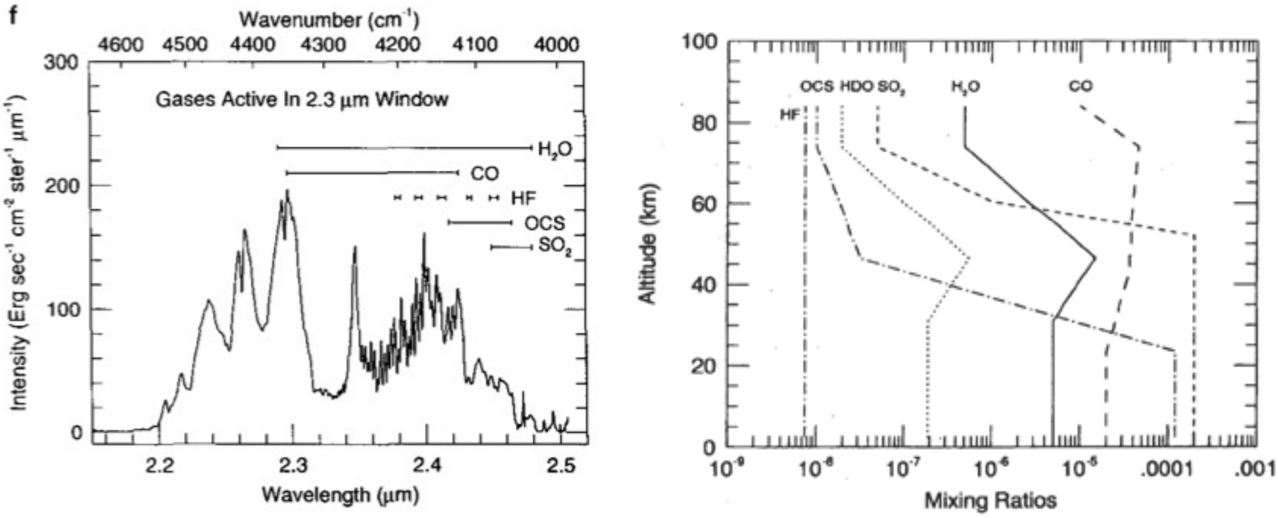

Pollack et al., Icarus 103, 1, 1993

Heating of Jupiter’s upper atmosphere above the Great Red Spot

Donoghue et al. (2016, Nature)

- infrared spectroscopy using SpeX spectrometer on the NASA Infrared Telescope Facility (IRTF)
- rotational-vibrational emission lines from H3+, a major ion in Jupiter’s ionosphere

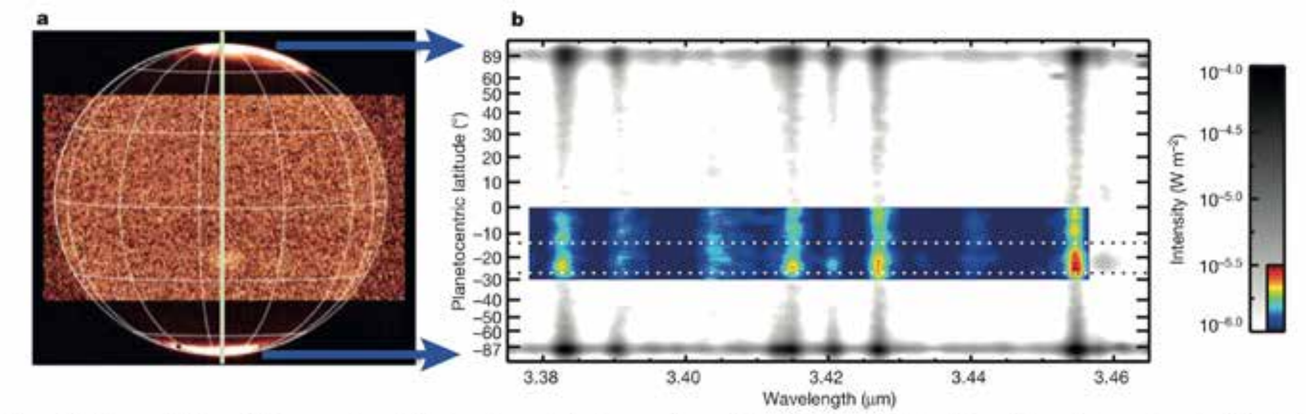

Figure 1 | The acquisition of Jovian spectra. a, Jupiter as observed by the SpeX slit-jaw imager and L-filter (3.13–3.53 μm), on 4 December 2012. Bright regions at the poles result from auroral emissions; the contrast at low and mid-latitudes has been enhanced for visibility. The vertical beige line in the middle of the image indicates the position of the spectrometer slit, which was aligned along the rotational axis. **b,** The co-added spectrum of seven GRS-containing exposures; dotted horizontal lines indicate the latitudinal range of the GRS. Further details are given in the Methods section.

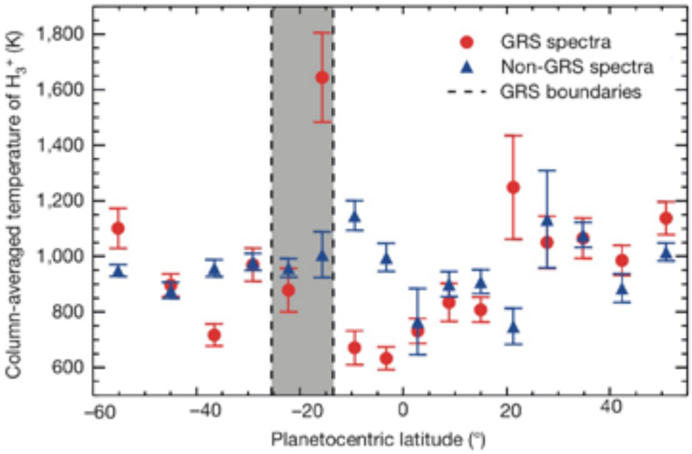

Figure 3 | Jovian H_3^+ temperatures versus planetocentric latitude. Column-averaged temperatures of H_3^+ shown here are each derived from model fits to the discrete H_3^+ emission lines as shown in Fig. 2. Red circle symbols correspond to the co-addition of GRS-related spectra (that is, from the spectral image in Fig. 1b) between 239° and 253° in Jovian system III Central Meridian Longitude (CML). The GRS latitudes are indicated by the grey shading. Blue triangle symbols were derived from exposures taken in the ranges 293°–359° and 0°–82° CML, that is, longitudes well separated from the GRS, representing the 'ordinary' background conditions based on solar heating alone. The modelled temperature of the upper atmosphere for these non-auroral regions is 203 K (ref. 1). Uncertainties are standard errors of the mean.

"This hotspot must be heated from below, and this detection is therefore strong evidence for coupling between Jupiter's lower and upper atmospheres, probably the result of upwardly propagating acoustic or gravity waves."

Total ozone mapping spectrometer(TOMS)

6 bands : 308.6, 312.5, 317.5, 322.3, 331.2, 360.0 nm

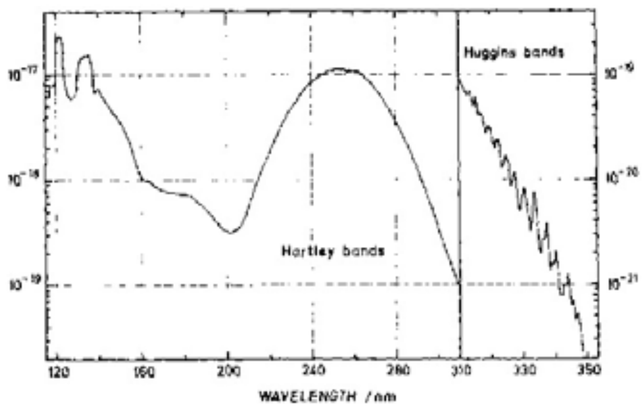

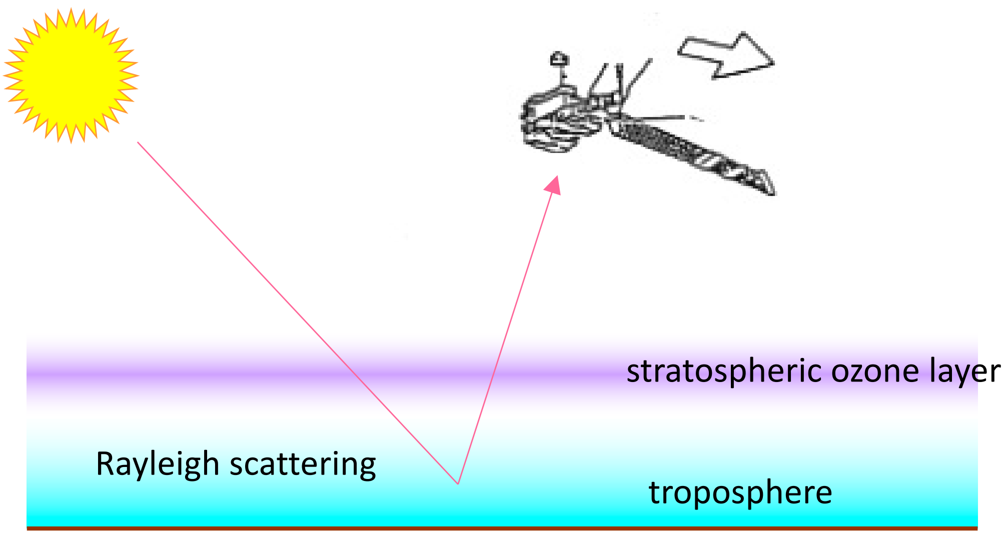

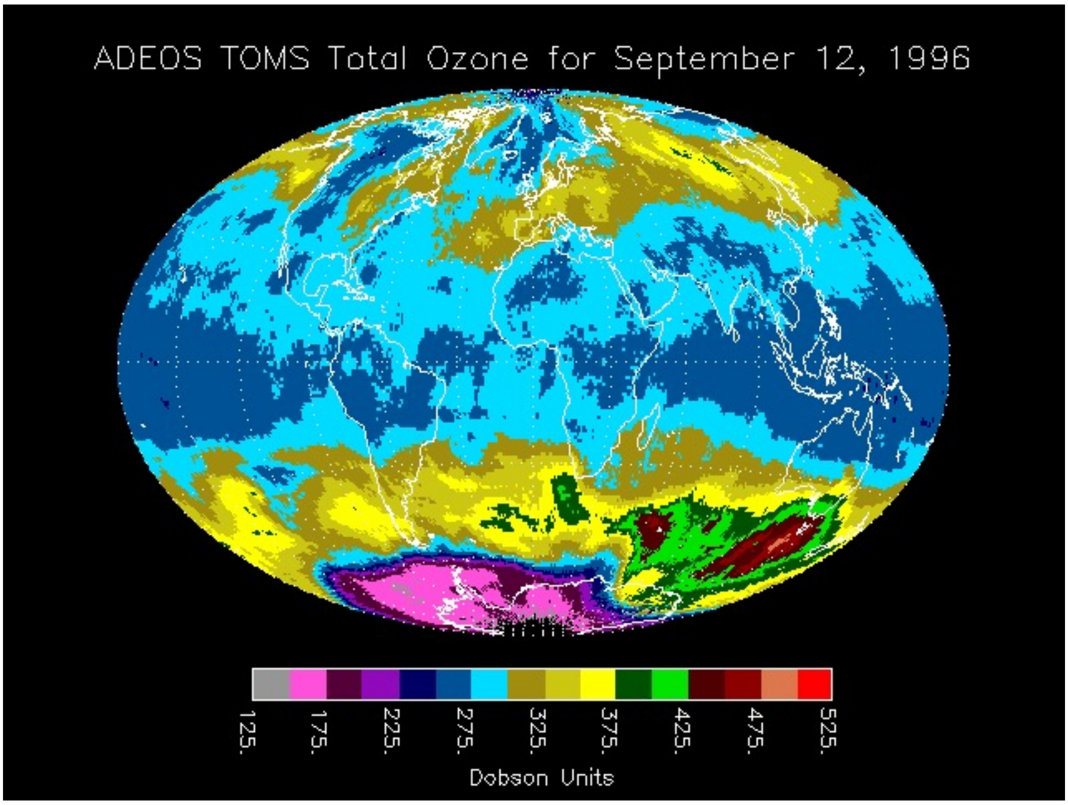

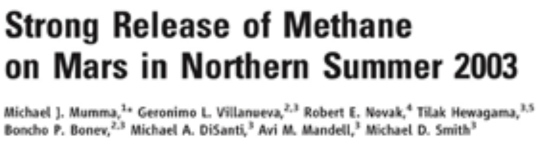
Strong Release of Methane on Mars in Northern Summer 2003

Michael J. Mumma,[1*] Geronimo L. Villanueva,[2,3] Robert E. Novak,[4] Tilak Hewagama,[3,5] Boncho P. Bonev,[2,3] Michael A. DiSanti,[3] Avi M. Mandell,[3] Michael D. Smith[3]

火星メタンの地上分光観測：
軌道運動によるDoppler shiftを利用

Mumma et al. (2009)

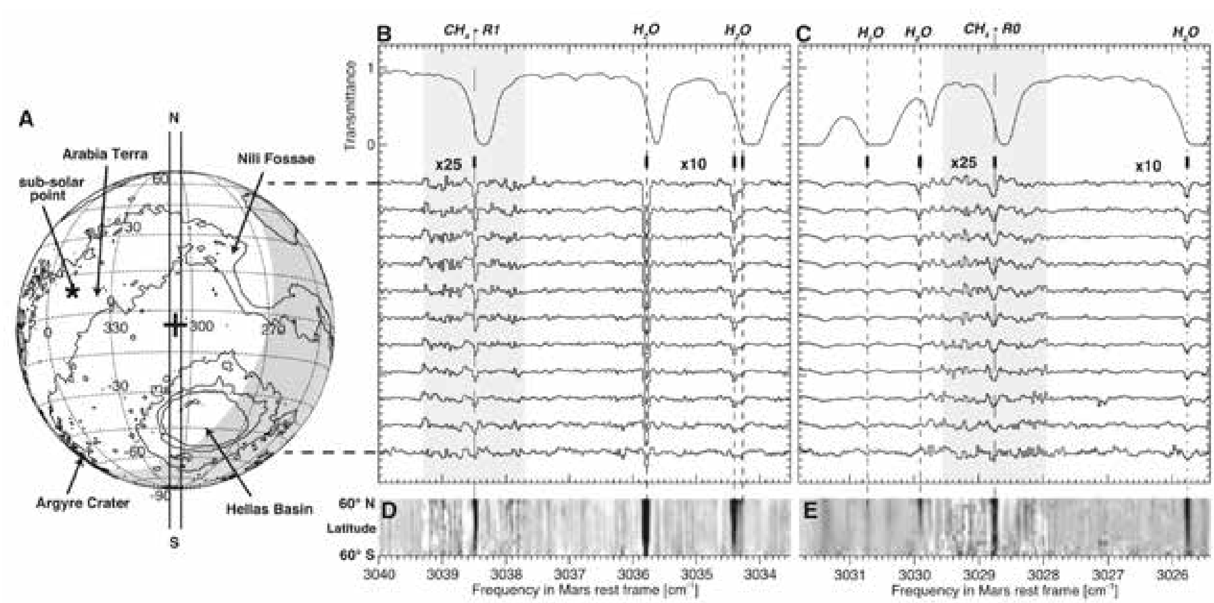

Mumma et al. (2009)

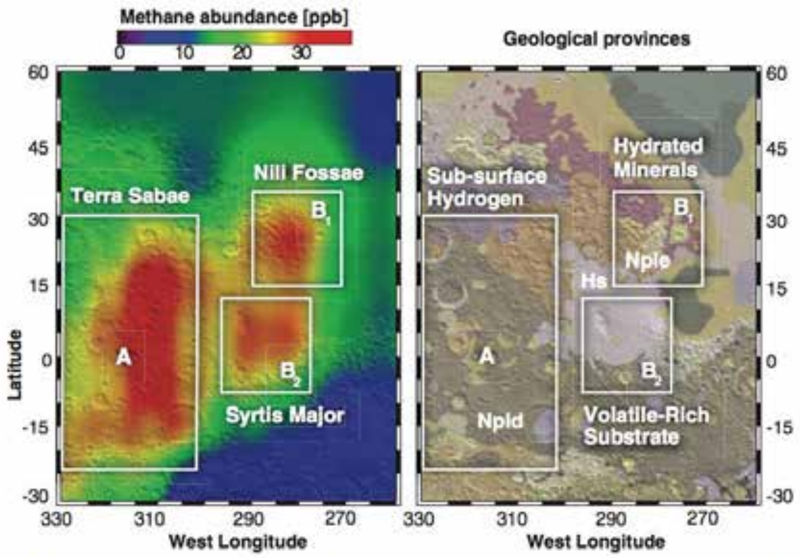

Fig. 3. Regions where CH_4 appears notably localized in northern summer (A, B_1, and B_2) and their relationship to mineralogical and geomorphological domains. **(A)** Observations of CH_4 near the Syrtis Major volcanic district. **(B)** Geologic map of Greeley and Guest (*45*) superimposed on the topographic shaded relief from the Mars Orbiter Laser Altimeter (*46*). The most ancient terrain units are dissected and etched Noachian plains (Npld and Nple) (~3.6 to 4.5 billion years old, when Mars was wet) and are overlain by volcanic deposits from Syrtis Major of Hesperian (Hs) age (~3.1 to 3.6 billion years old).

Martian water vapor: Mars Express PFS/LW observations of thermal infrared emission

Fouchet et al. (2007)

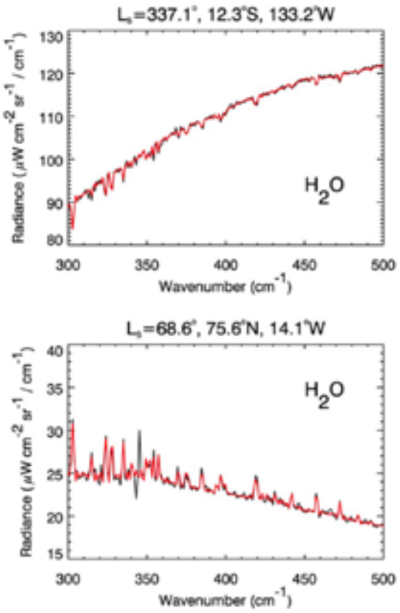

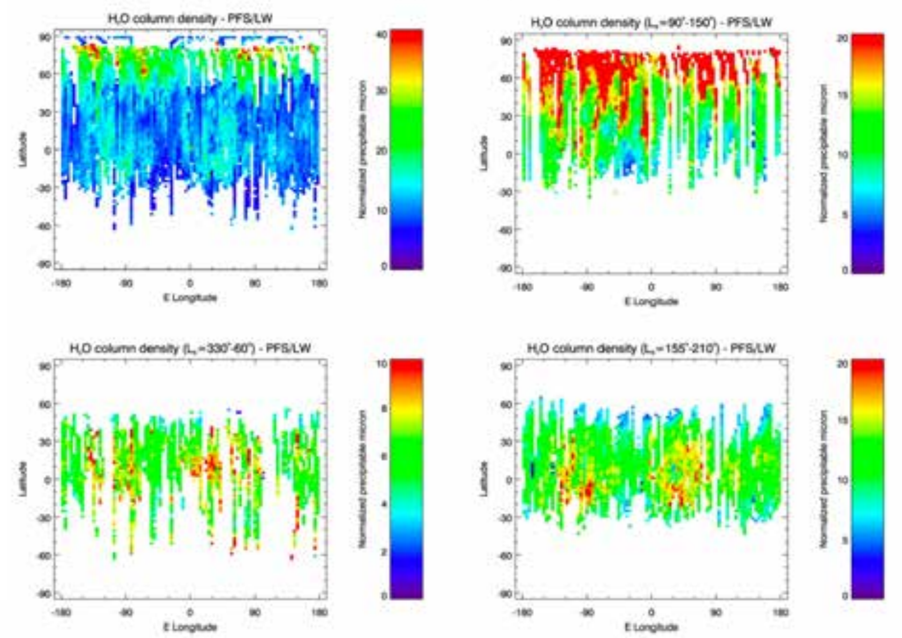

Fig. 6. Geographical distribution of water. Water columns are here normalized to a common 610 Pa pressure. Top left: entire dataset. Top right: $L_s = 330°$–$60°$. Bottom left: $L_s = 90°$–$150°$. Bottom right: $L_s = 155°$–$210°$.

Doppler wind measurements of the Venusian thermosphere from sub-millimeter CO absorption line observations

Clancy et al. (2012)

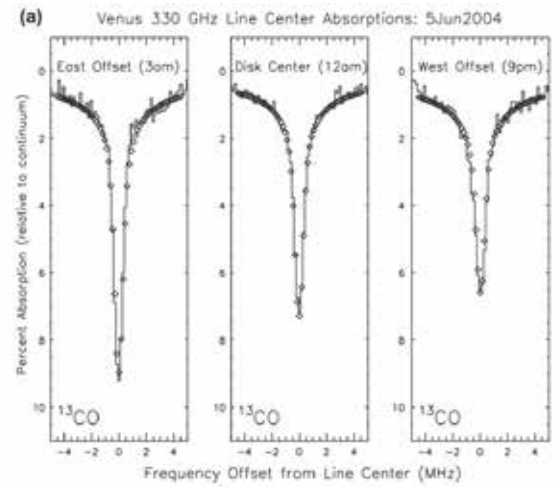

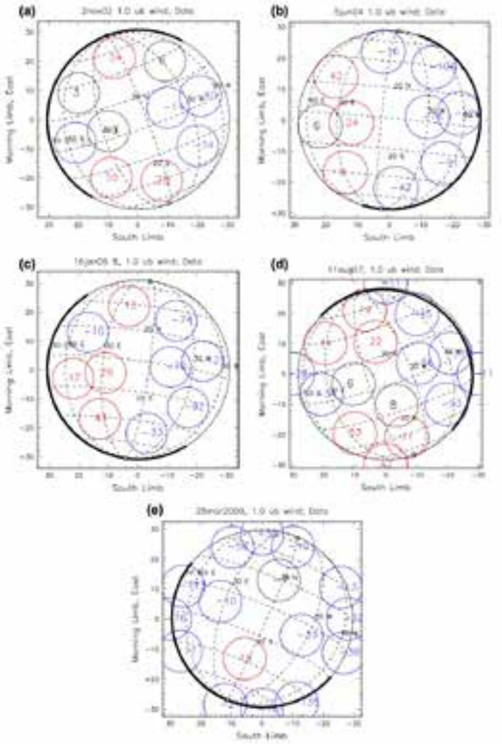

Fig. 7. The distribution and amplitude of fitted Doppler wind velocities (m/s) at the 1 μbar pressure level (~109 km altitude) are indicated for beam integration positions across the nightside apparent disk at Venus inferior conjunctions on November 2, 2002 (a), June 5, 2004 (b), January 16, 2006 (c), August 11, 2007 (d), and March 28, 2009 (e). Negative (blue) values refer to approaching Doppler winds, positive (red) values refer to receding Doppler winds. Values falling within the 1σ measurement uncertainty (10 m/s at 1 μbar) are indicated by black circles. The diffraction FWHM resolution of each observation is indicated by the circles (14 arcsec). Relatively weak nightside lower thermospheric wind velocities, poorly described by SSAS or zonal circulation, are apparent in (a). Nightside wind velocities consistent with retrograde zonal and SSAS circulation are apparent in (b). Complex zonal and SSAS circulation is apparent in (c) and (d), versus primarily SSAS circulation in (e). (For interpretation of the references to color in this figure legend, the reader is referred to the web version of this article.)

Limb sounding of Earth’s stratosphere：ISS/SMILES

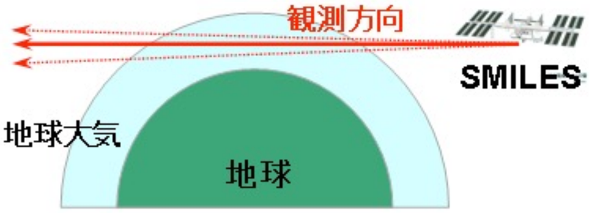

spectroscopy of far-infrared emission

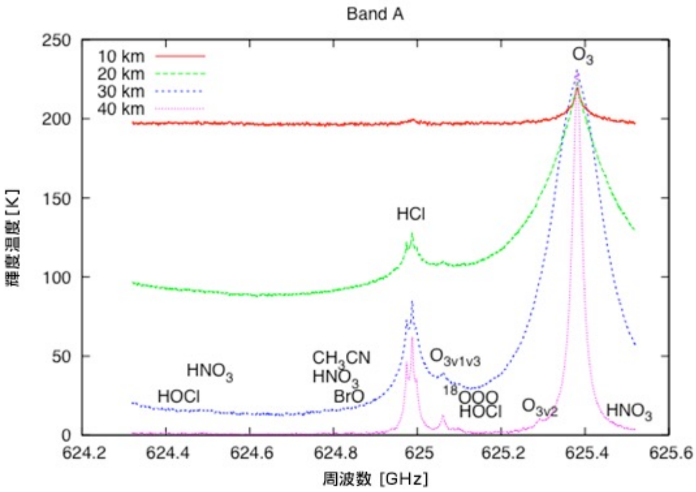

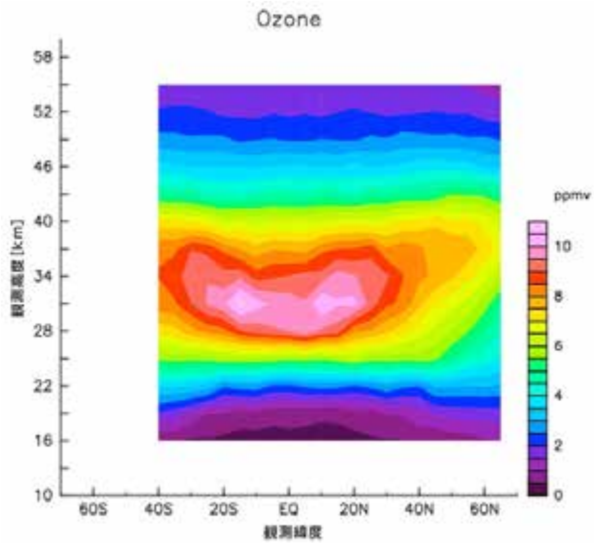

Stellar occultation : Venus Express/SPICAV

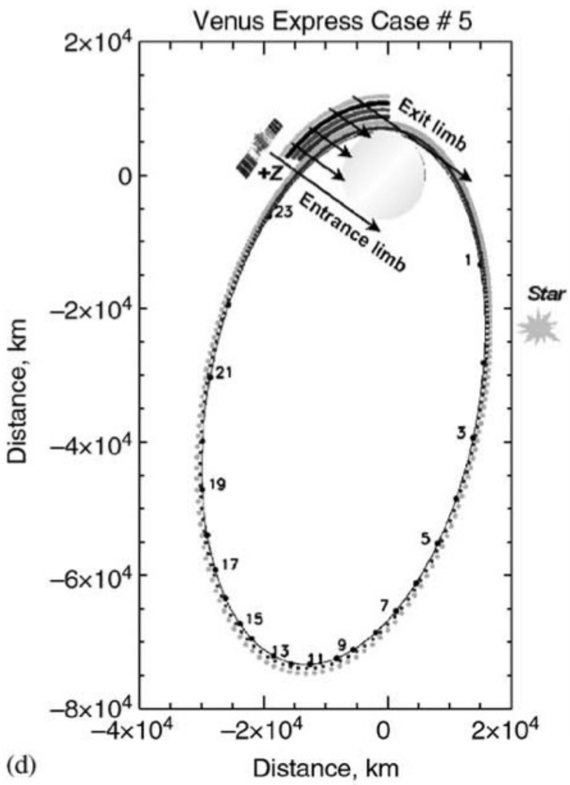

Using stars as the light source

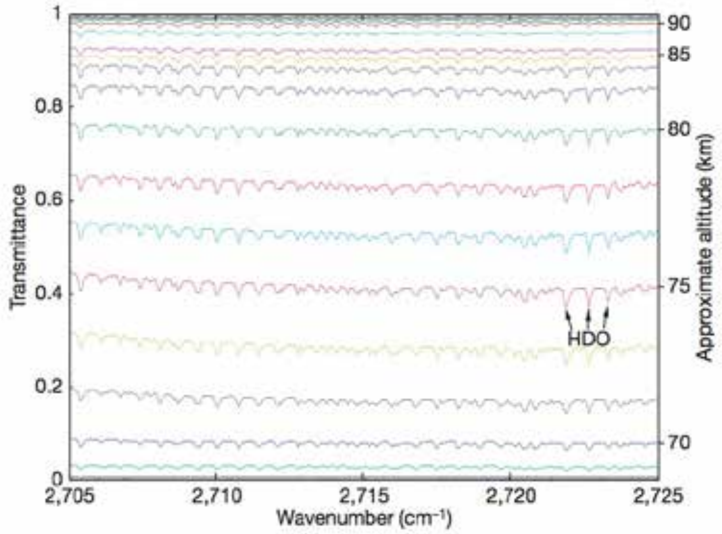

Figure 2 | Typical evolution of atmospheric spectral transmittances through one solar occultation observed by SOIR spectrometer. It is obtained by

Venus Express/SPICAV

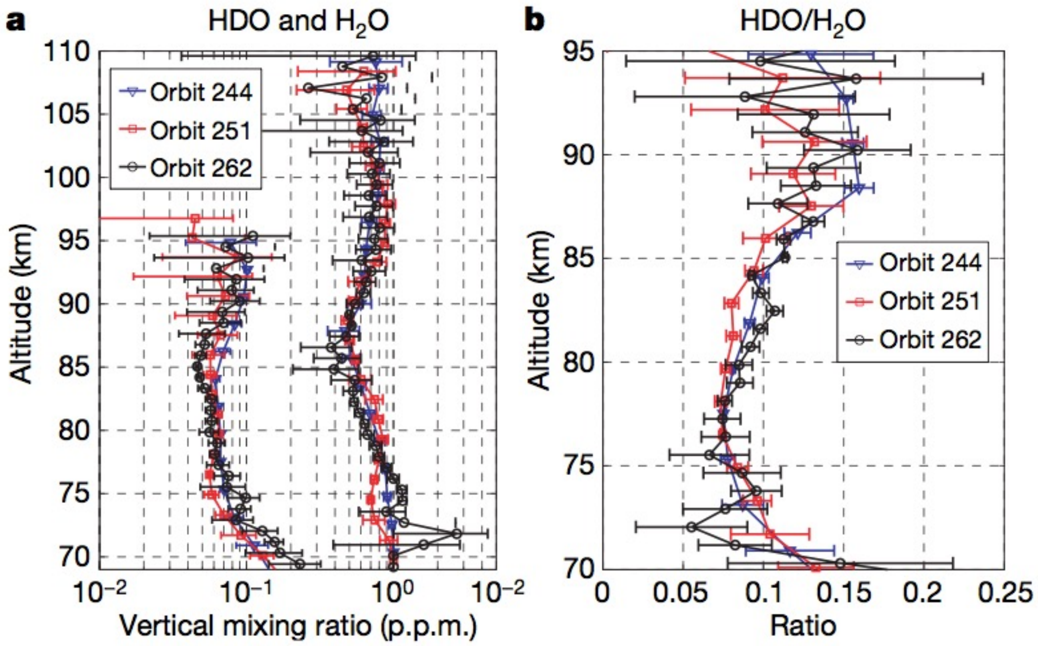

Figure 4 | HDO and H_2O mixing ratio, HDO/ H_2O vertical profiles. Both

SO, SO_2 profiles above cloud observed by Venus Express solar occultations (Belyaev et al. 2011)

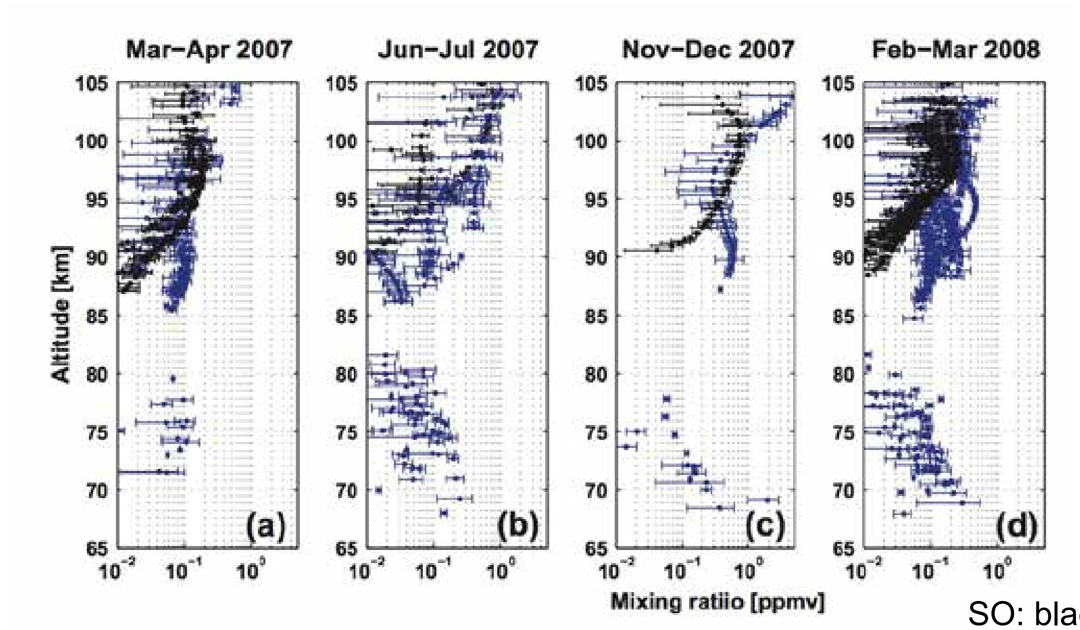

SO: black
SO_2: blue

- Enhancement at high altitudes cannot be explained by traditional photochemical models.

Mars Climate Sounder on Mars Reconnaissance Orbiter

McCleese et al. (2007)

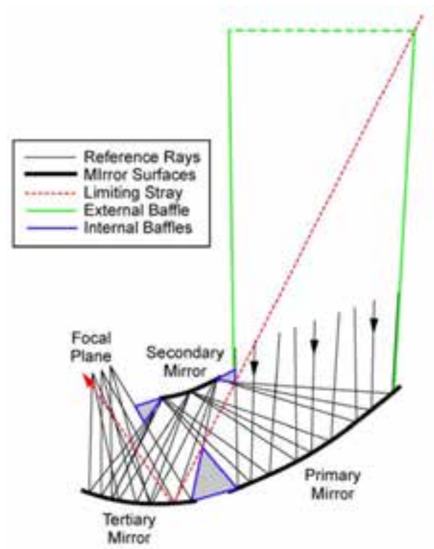

Figure 4. MCS telescope optical schematic and baffle approach.

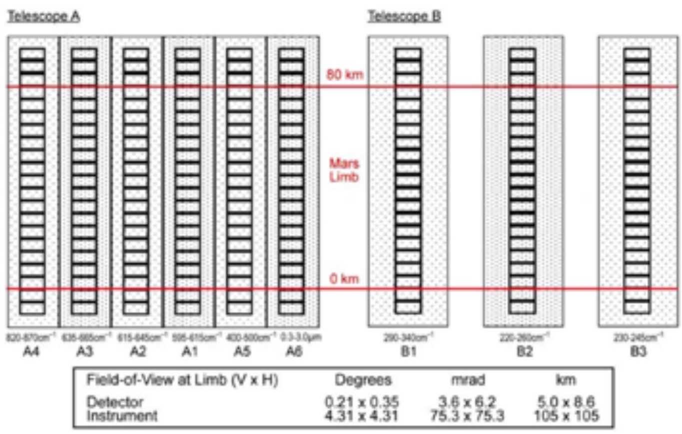

Figure 3. MCS fields of view projected at the limb of Mars. The telescope A and B FOV responses are aligned to be superimposed within one-half FOV in the horizontal dimension and one-tenth FOV in the vertical (shown separated in figure for clarity).

Meridional cross section of dust mixing ratio

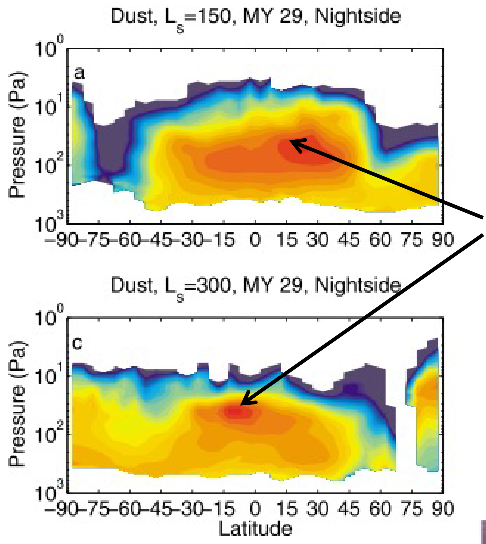

Detached dust layers

Heavens et al. (2011)

“Rocket dust storm”: source of high-altitude dust ?

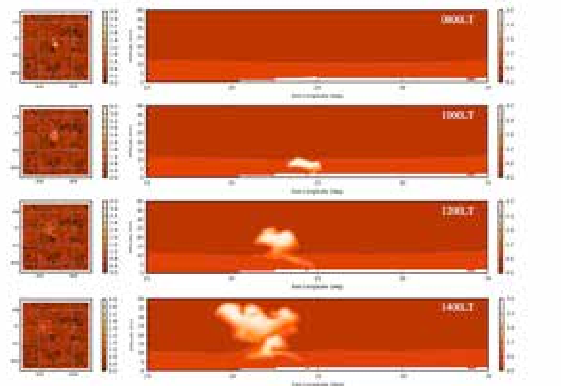

Spiga et al. (2013)

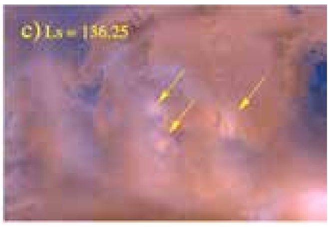

Previous observations failed to detect temporal development of localized dust plumes that might play crucial roles in distributing the background dust

“Limb-viewing” spectroscopy of exoplanets

- Transit spectroscopy

Kreidberg (2018)

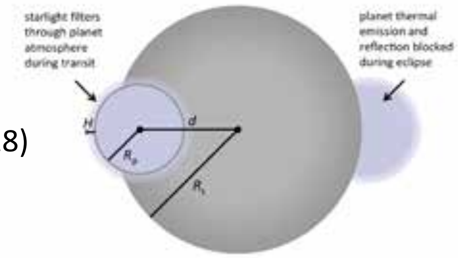

Howe & Burrows (2018)

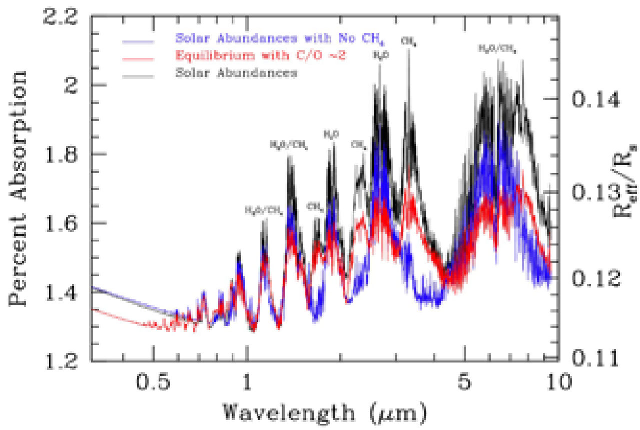

hydrogen-rich atmospheres with non-solar relative abundances

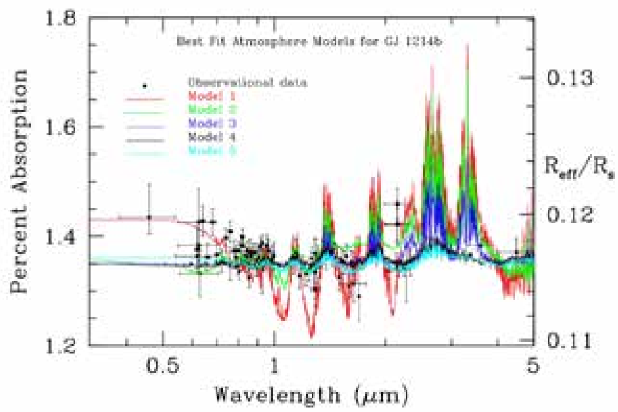

Models 1-3 use a solar-abundance atmosphere, while Models 4 and 5 use an atmosphere of 1% H_2O and 99% N_2

Radio observations of planetary atmospheres

Merit of radio observation

- Techniques of high-precision frequency measurements are available. This enables high-precision retrieval of atmospheric structures.
- Facilities for deep-space telecommunication can (sometimes) be used for the observations. This saves weight resources of spacecraft.

- Two types of observations will be introdued:
  - Radio occultation (active method)
  - Spectroscopy/radiometer (passive method)

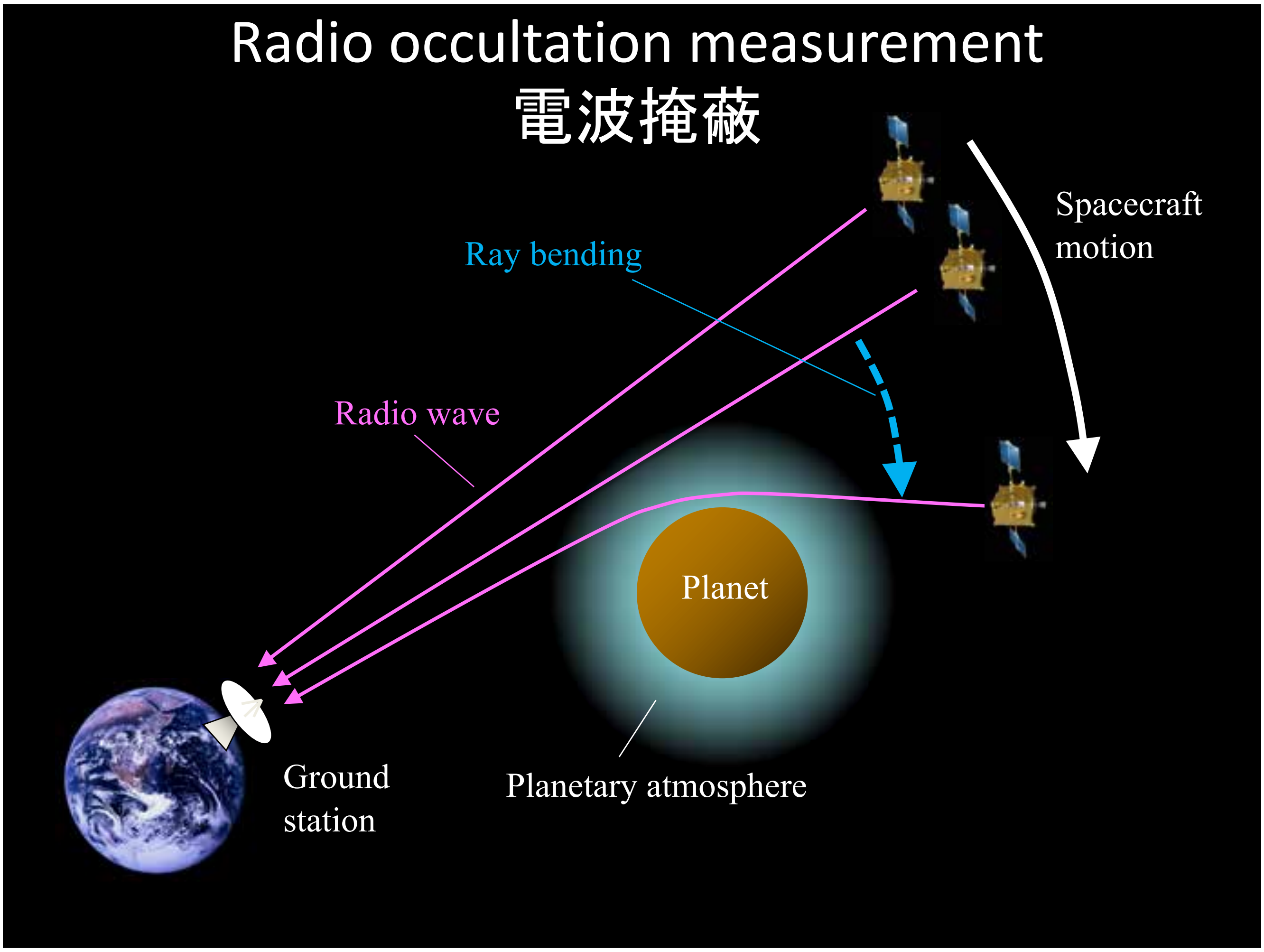

Ultra-Stable Oscillator (USO) on Akatsuki

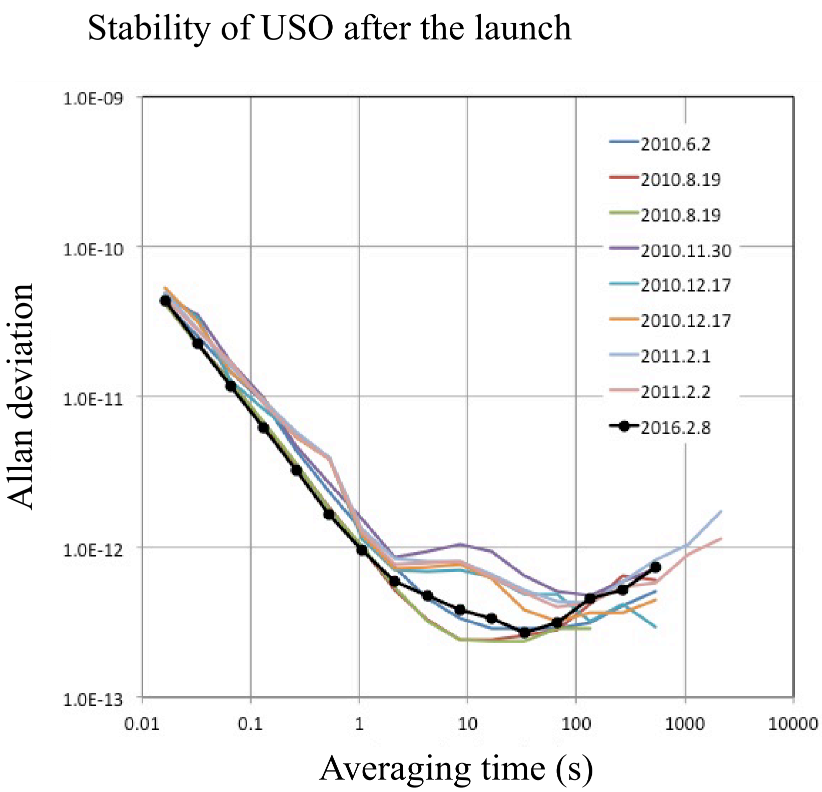

USO on Akatsuki

The requirement (Allan dev < 1×10^{-12} for τ = 1-1000 s) is satisfied.

High-gain antenna

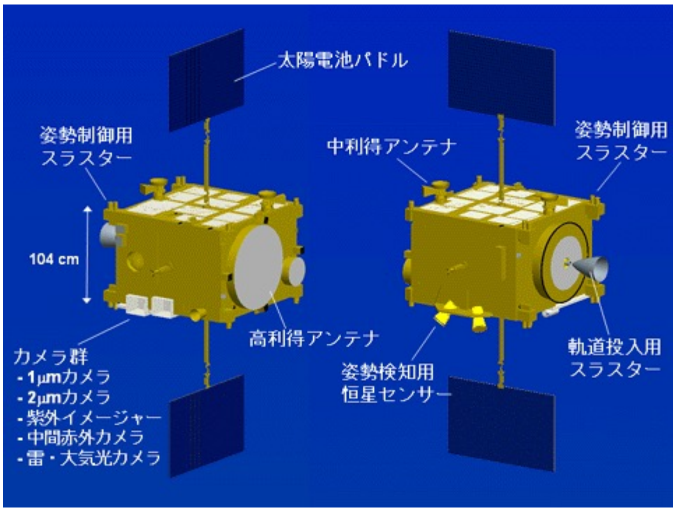

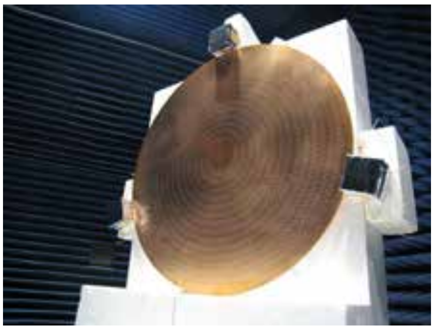

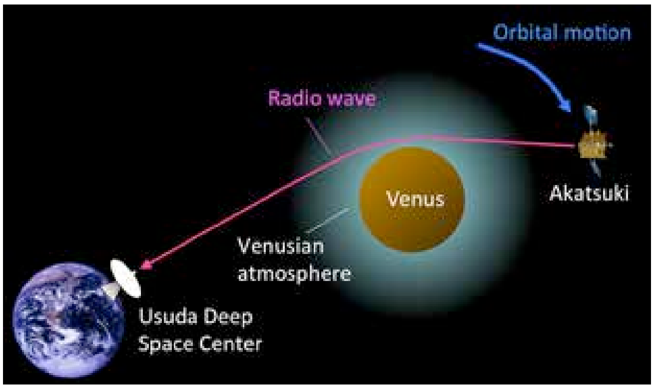

Attitude maneuver is needed during experiments due to ray bending

Data acquisition

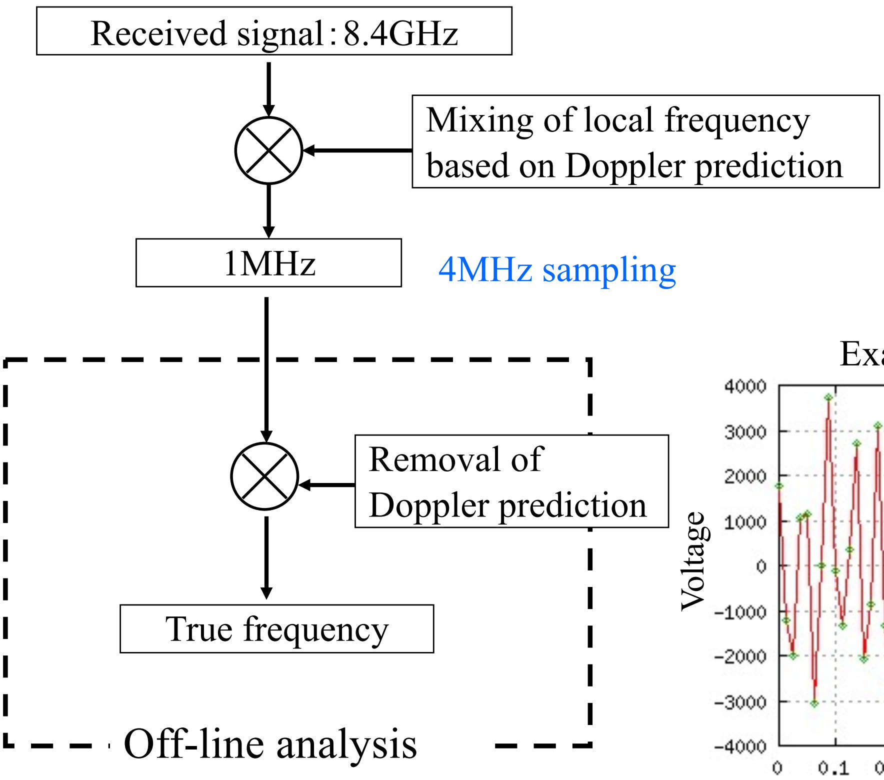

Usuda Deep Space Center (UDSC)

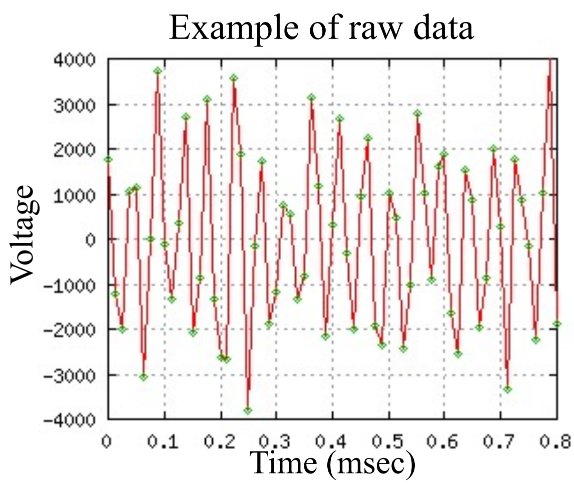

Spectrum of radio wave from Venus orbiter Akatsuki

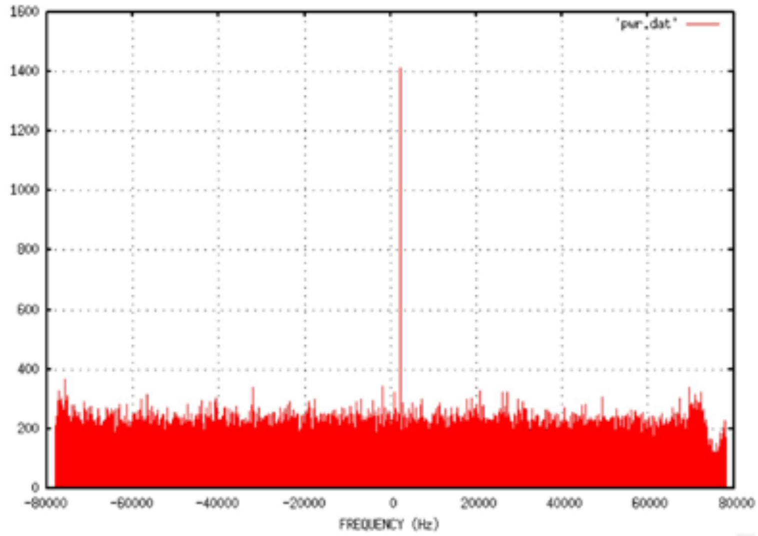

Signal spectrum with 1-sec integration reproduced from data in RDEF format at JAXA

Radio occultation measurement

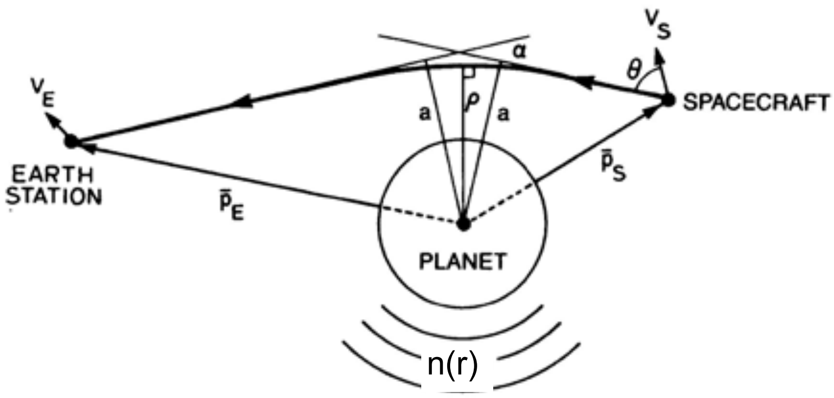

a : Impact parameter

α : Bending angle

n : Refractive index

r : Distance from planet center

Tyler (1987)

$$\alpha(a) = -2a \int_{r=r_0}^{r=\infty} \frac{1}{n}\frac{\partial n}{\partial r}\frac{dr}{\sqrt{(nr)^2 - a^2}}$$

Abel transformation:

$$\pi \ln n(r_{01}) = -\int_{a=a_1}^{a=\infty} \frac{\alpha(a)}{\sqrt{a^2 - a_1^{\,2}}}\, da$$

Refractive index n is related to atmospheric structure:

$$\mu(r) = (n(r)-1)\times 10^6 \qquad : \text{Refractivity}$$

$$= \underbrace{\boxed{\kappa N_n(r)}}_{\text{neutral atmosphere}} - \underbrace{\boxed{40.3\frac{N_e(r)}{f_0^2}\times 10^6}}_{\text{plasma}}$$

Retrieval of the neutral atmosphere's temperature based on hydrostatic equilibrium:

$$T(r) = \frac{N_n(r_{top})}{N_n(r)}T(r_{top}) + \frac{\overline{m}}{kN_n(r)}\int_r^{r_{top}} N_n(r')g(r')dr$$

- Temperature at the upper boundary should be given from empirical models. The effect of the upper boundary almost disappears 1-2 scale heights below the boundary.

Retrieval procedure

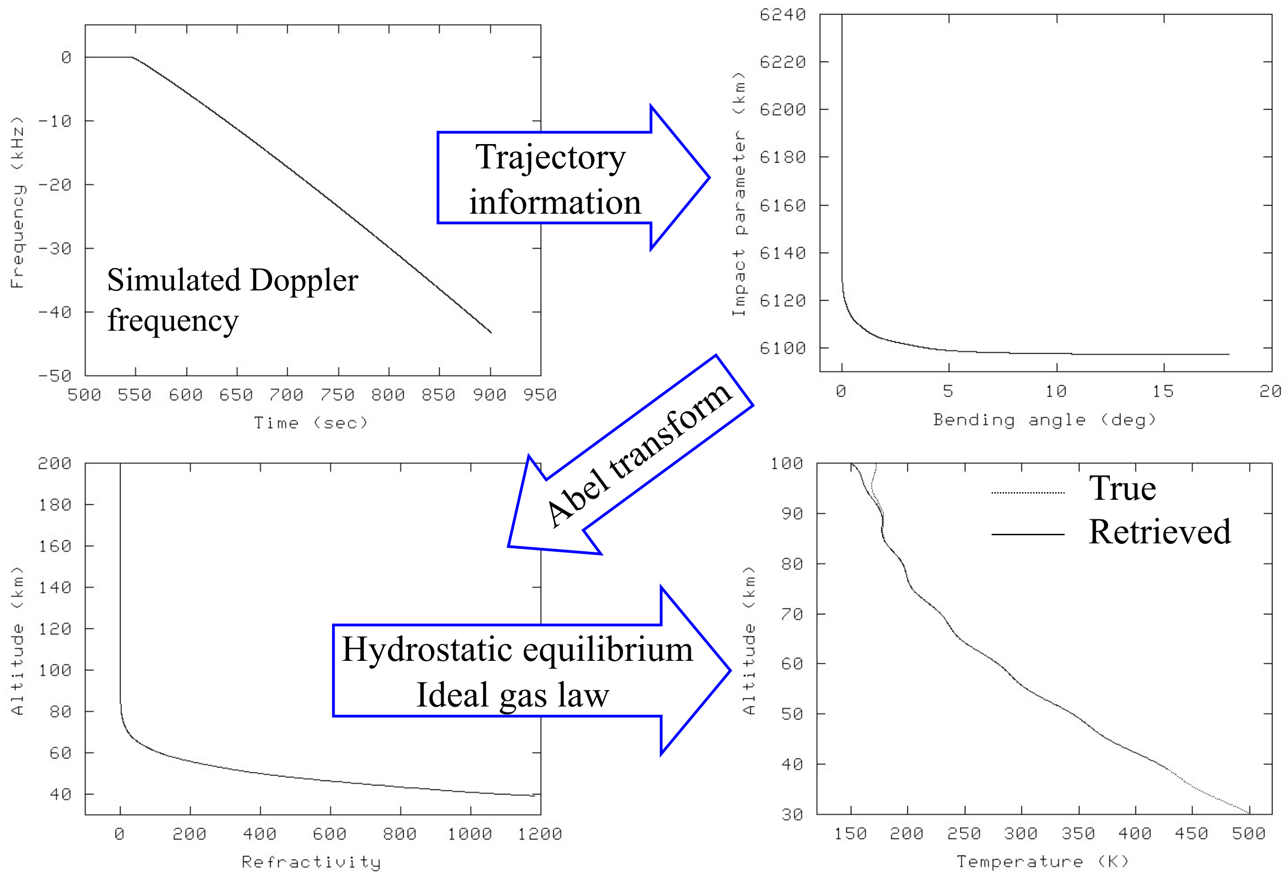

Temperature profiles of the Venus atmosphere obtained by Akatsuki radio occultation

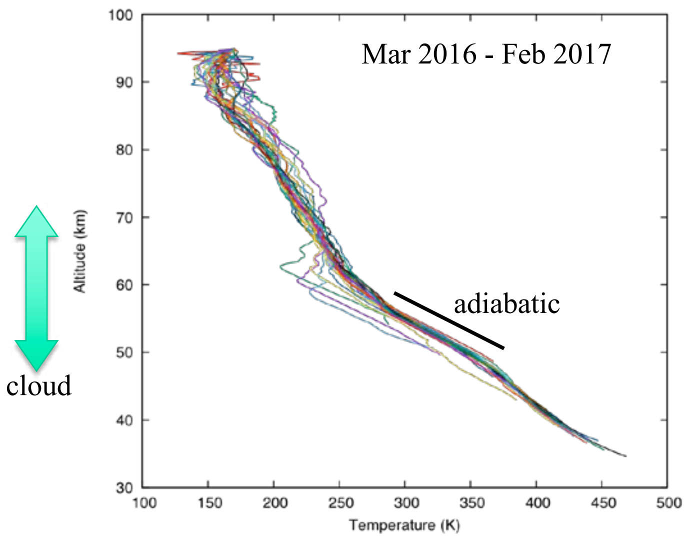

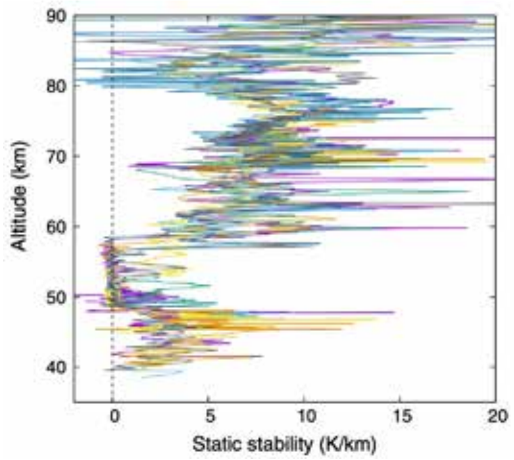

Imamura et al. 2017

static stability: $S = \frac{dT}{dz} - \frac{g}{c_p}$

T : temperature
z : altitude
g : gravitational acceleration
c_p : specific heat for constant pressure

limitation of vertical resolution

$$F_n = \sqrt{\frac{n\lambda d_1 d_2}{d_1 + d_2}}, \quad d_1, d_2 \gg n\lambda,$$ [3]

where

F_n is the nth Fresnel zone radius,
d_1 is the distance of P from one end,
d_2 is the distance of P from the other end,
λ is the wavelength of the transmitted signal.

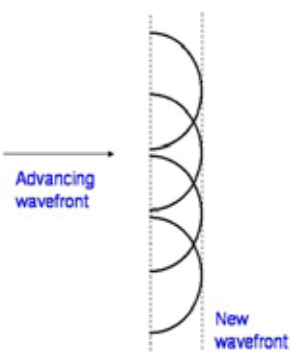

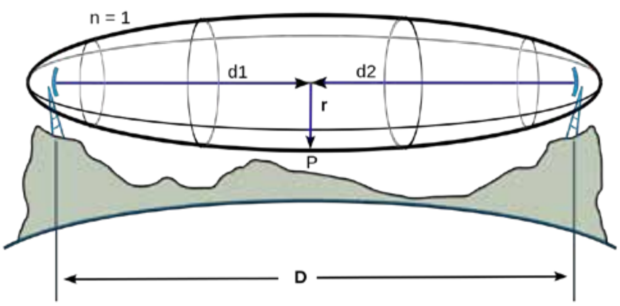

(Wikipedia)

n = 1 : First Fresnel zone. Outside this zone a destructive inference greatly reduces the contribution to the received signal.

F_1 is typically several hundred kilometers for interplanetary missions.

Multipath

An example of the signal spectrum time series (Imamura et al. 2018)

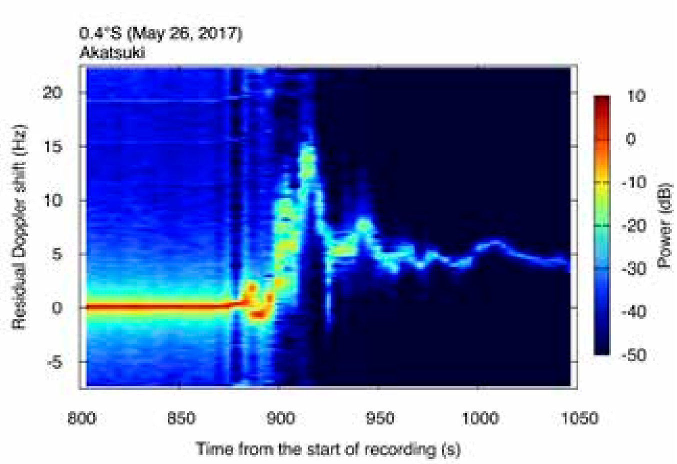

Schematic of multipath (Sokolovskiy, 2004)

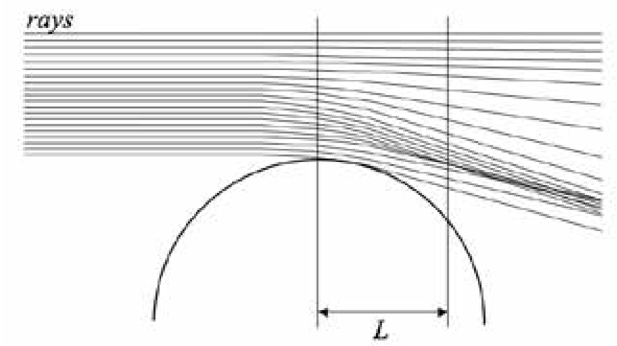

Radio holographic method can solve multipath problem.

Radio holographic analysis

- One of the radio holographic methods, FSI ("Full Spectrum Inversion" Jensen et al. 2003) is applied to RS data.
- Spectral analysis is applied to the entire signal at once instead of applying it to successive short time blocks.

→High vertical resolution + Disentanglement of multipath

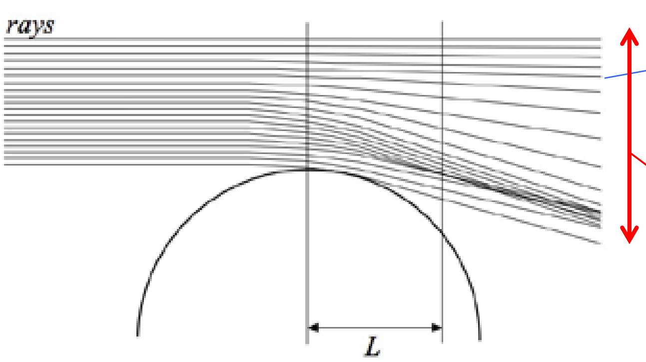

GO (geometrical optics) solves the instantaneous ray path at each time step

FSI solves the whole time series of the signal phase at once

Schematic of multipath (Sokolovskiy, 2004)

Examples

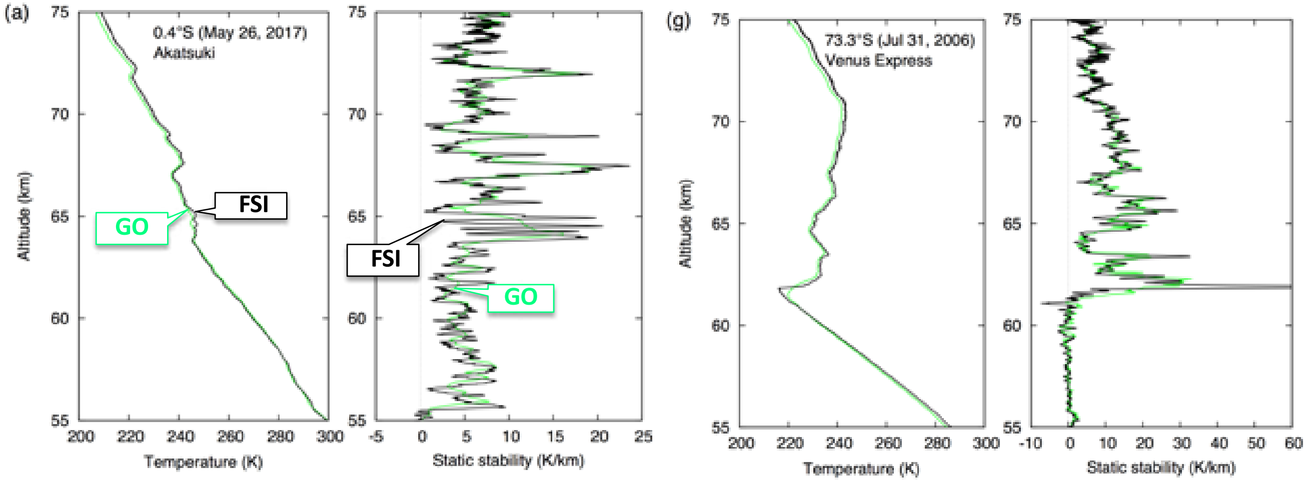

Imamura et al. (2018)

Radio occultation of lunar photoelectron layer with SELENE

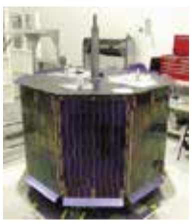

Vstar subsatellite

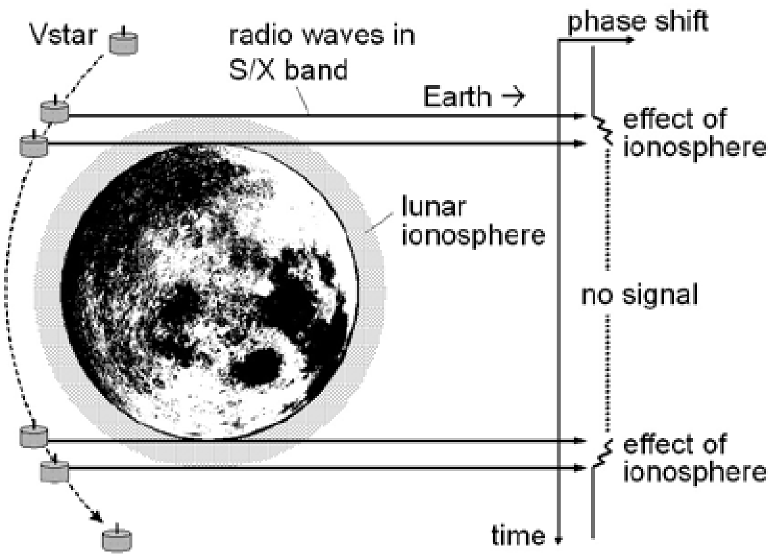

Usuda Deep Space Center, Japan

Dual-frequency method

To remove the effect of the fluctuation of the transmitted signal's frequency and the neutral atmosphere's contribution, two frequencies generated from the common onboard oscillator are used. A linear combination of these phases can extract the plasma contribution.

$$\Delta\phi_S = -\frac{40.3}{c\, f_S} N_e + \alpha\, f_S$$: Phase shift of S-band

$$\Delta\phi_X = -\frac{40.3}{c\, f_X} N_e + \alpha\, f_X$$: Phase shift of X-band

$$\delta\phi = \Delta\phi_S - \frac{f_S}{f_X}\Delta\phi_X = -\frac{40.3}{c} f_S \left(\frac{1}{f_S^2} - \frac{1}{f_X^2} \right) \cdot N_e$$: Differential phase

Analysis procedure

Phase deviation in S-band (ϕ_S) and X-band (ϕ_X)

Differential phase $\phi_{diff} = \phi_S - f_s/f_x\, \phi_X$
(f_s, f_x : S/X-band nominal freq.)

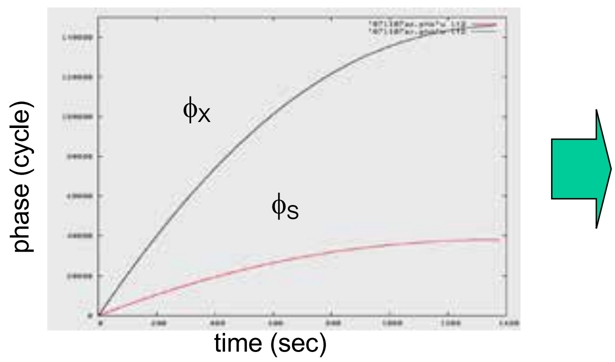

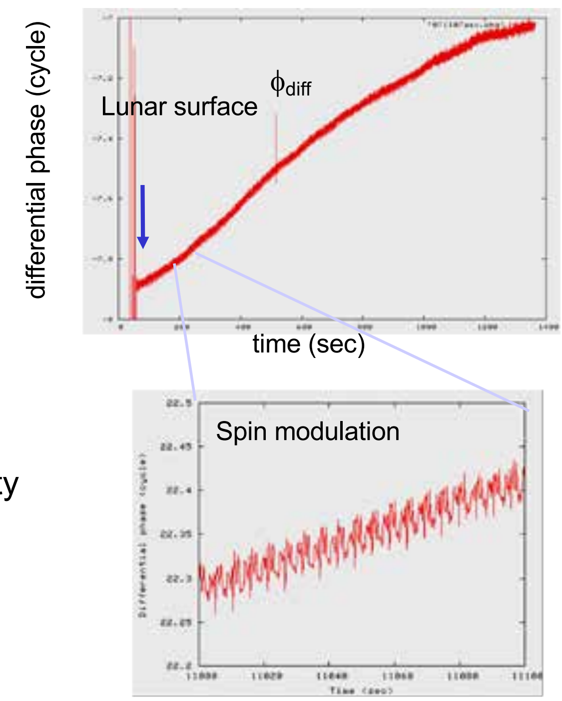

ϕ_{diff} is proportional to the electron density integrated along the ray path.

Mean density profile at SZA<60°

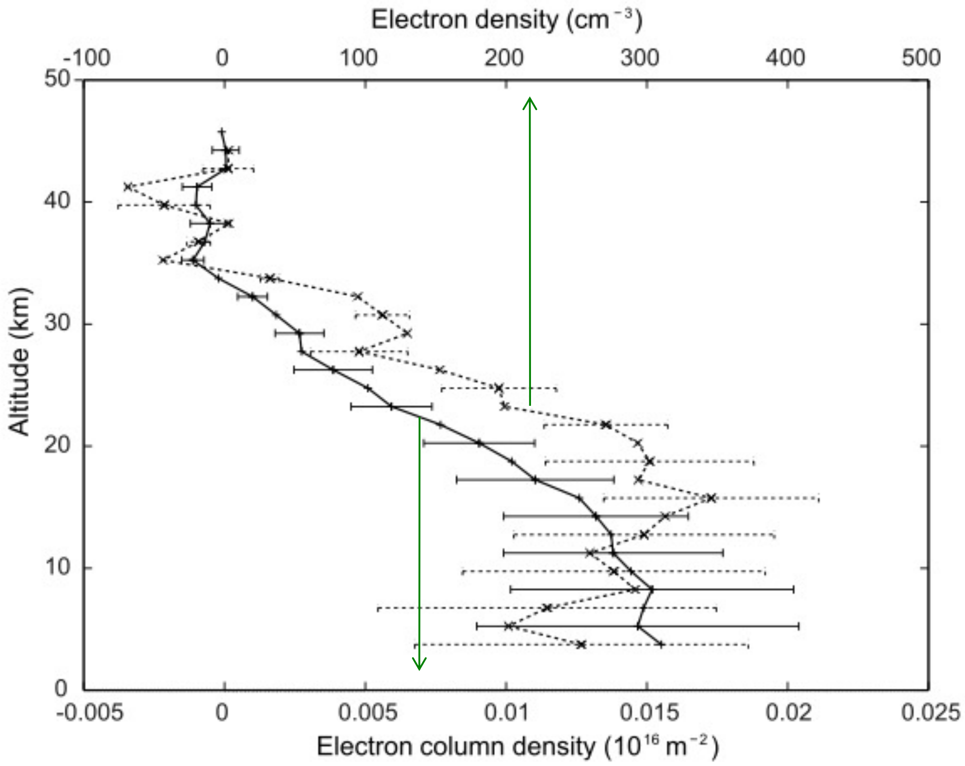

Imamura et al. (2012, JGR)

Examples of Venus' electron density profile from Akatsuki radio occultation

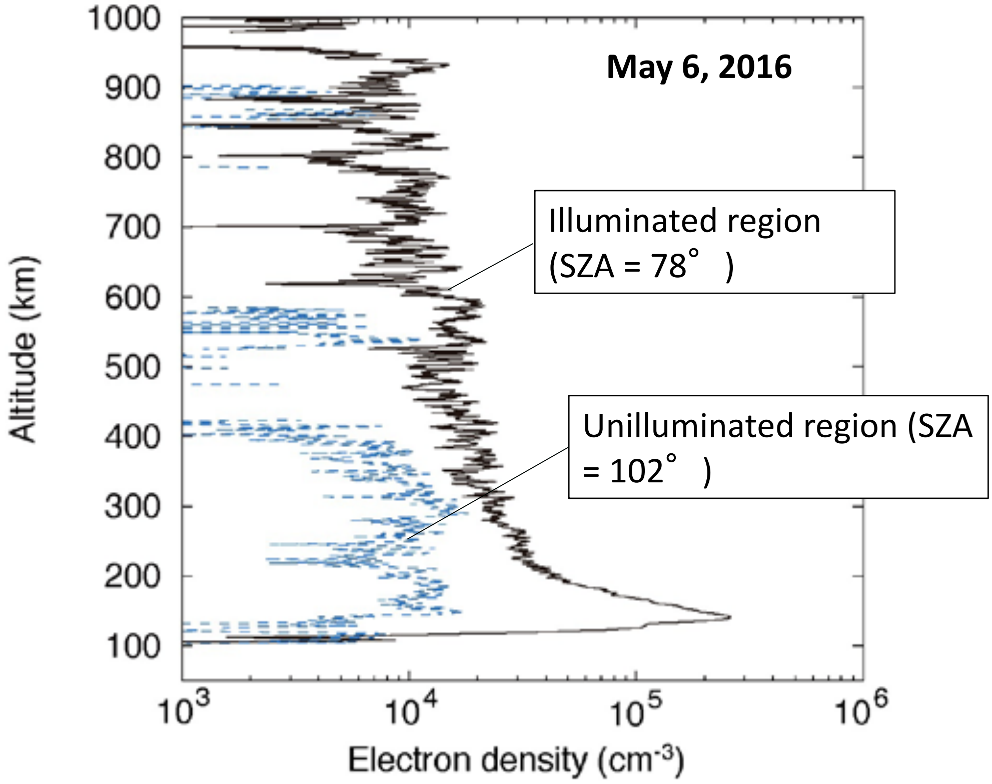

GPS meteorology for Earth

UCAR/COSMIC homepage

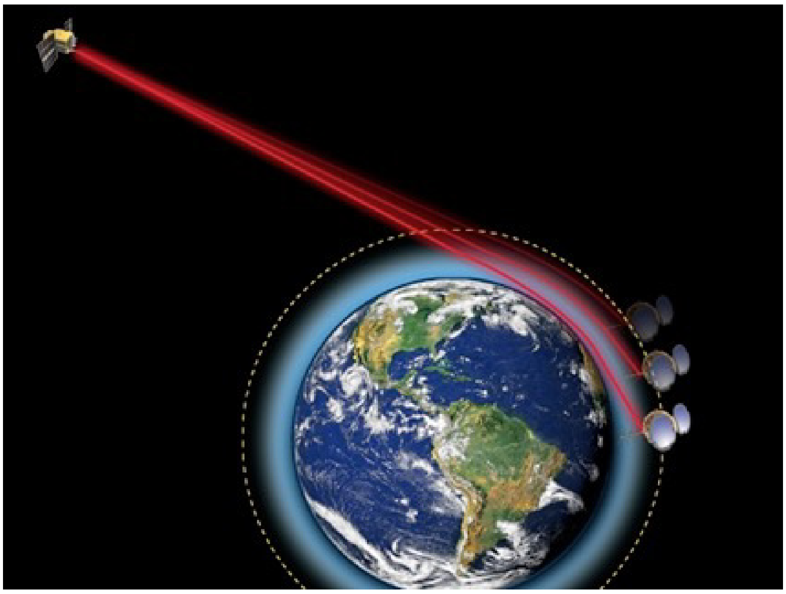

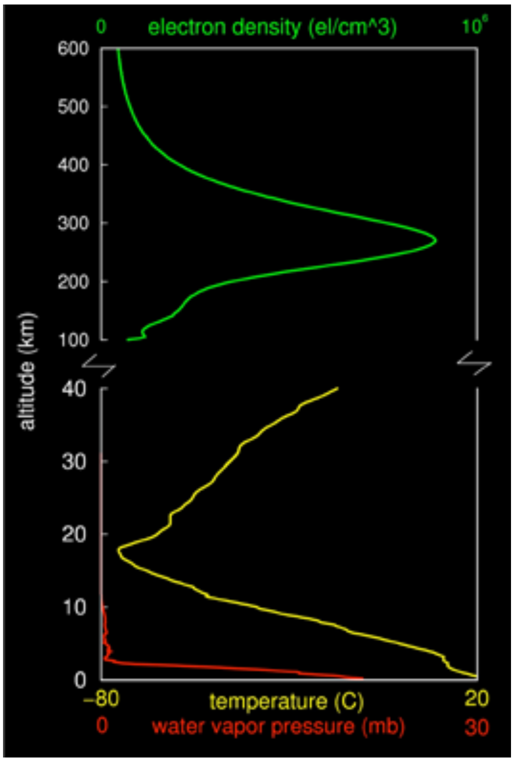

COSMIC : Constellation Observing System for Meteorology, Ionosphere, and Climate

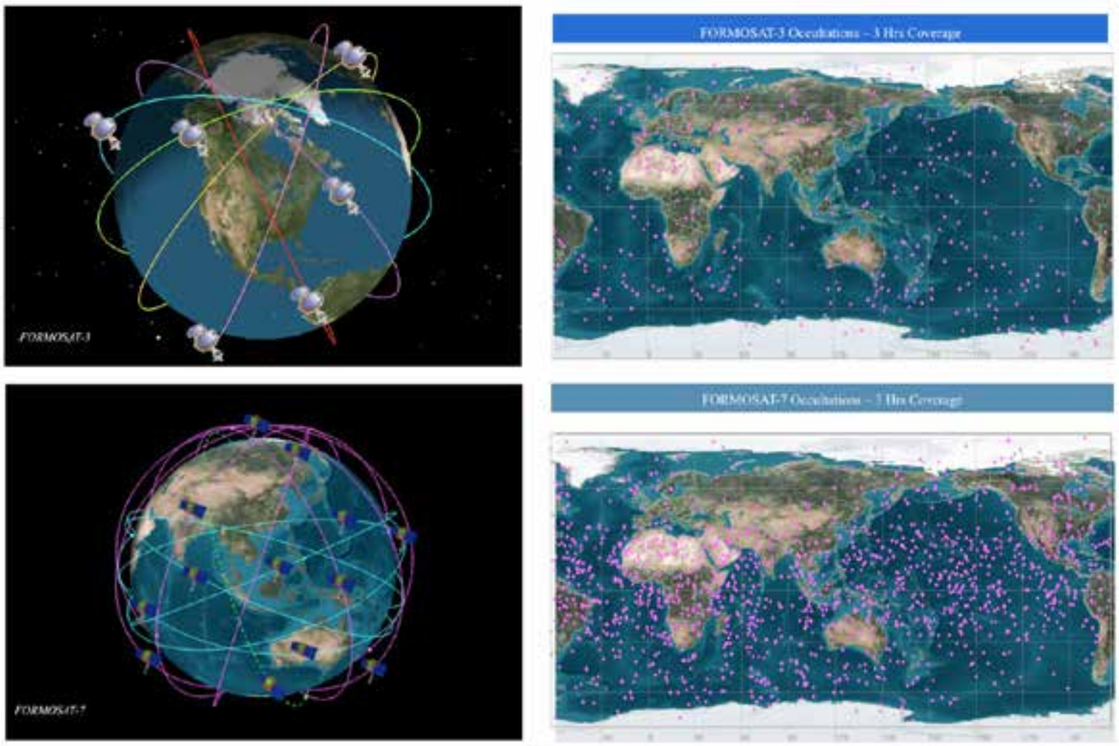

UCAR/COSMIC homepage

Fig. 1. Constellation design and estimated distribution of GPS RO soundings over a 3-h period from COSMIC/FORMOSAT-3 and COSMIC-2/FORMOSAT-7. The first tropical constellation of COSMIC-2 will be launched in 2016, and the second constellation will be launched in 2018. COSMIC-2 will provide an order of magnitude more GPS RO soundings over the tropics, which will have a significant impact on tropical cyclone prediction.

Dual-orbiter planetary mission

Satellite-to-satellite radio occultation and atmospheric spectroscopy for understanding vertical transport of water, dust and minor gases which controls climate evolution

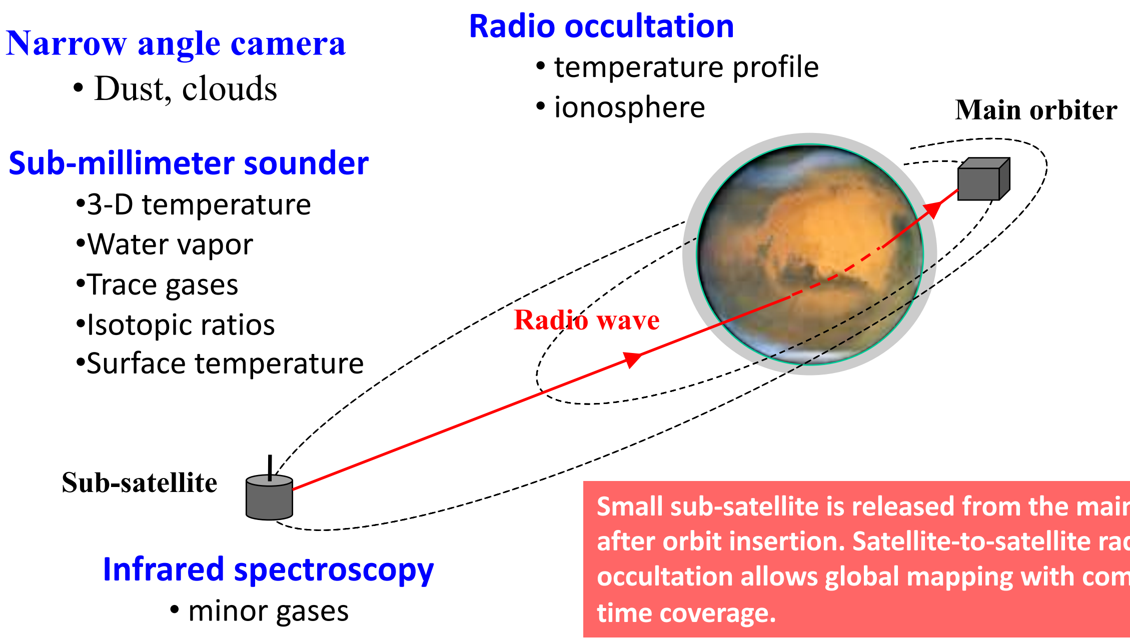

Small sub-satellite is released from the main orbiter after orbit insertion. Satellite-to-satellite radio occultation allows global mapping with complete local-time coverage.

Radio scintillations caused by planetary atmospheres and the solar corona

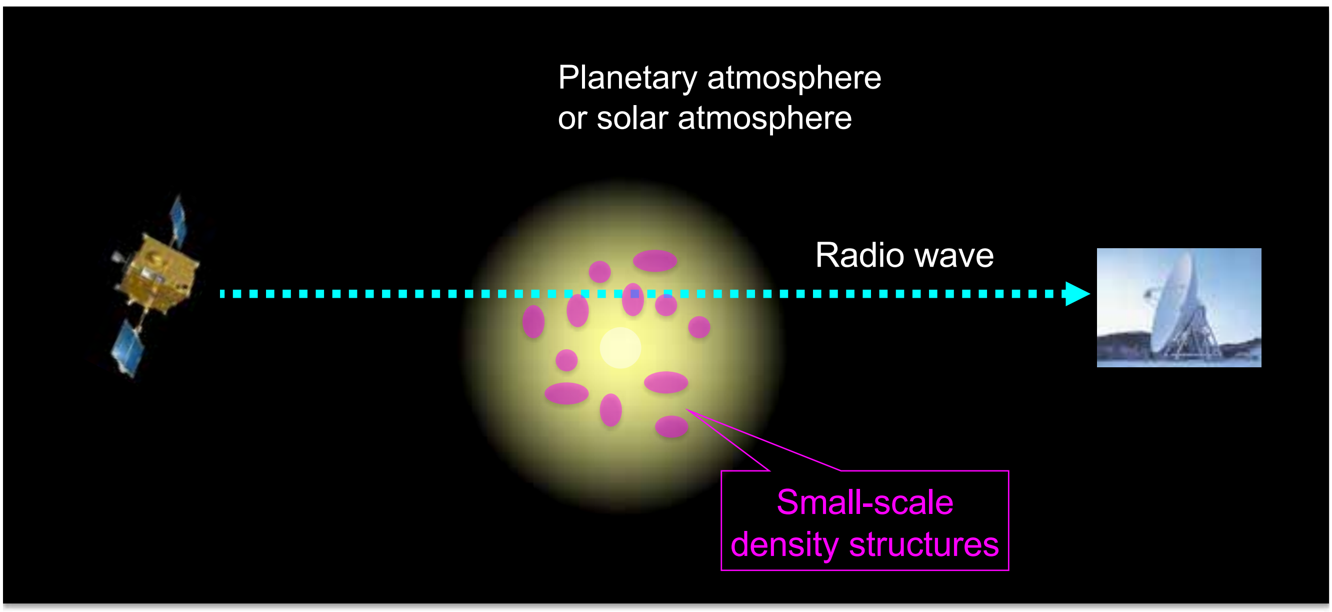

Radio scintillation measurement

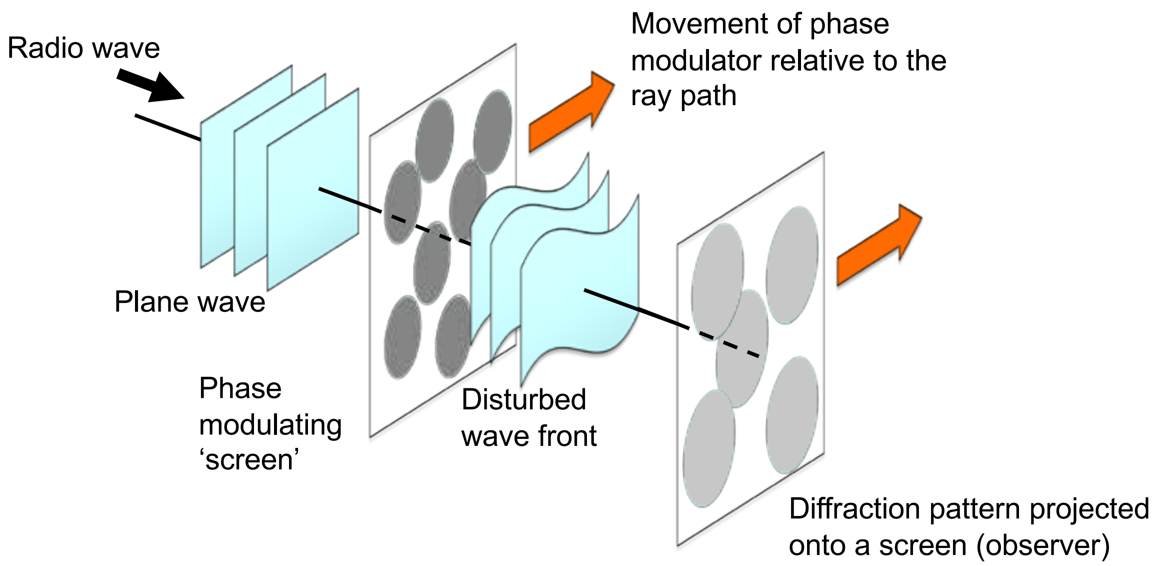

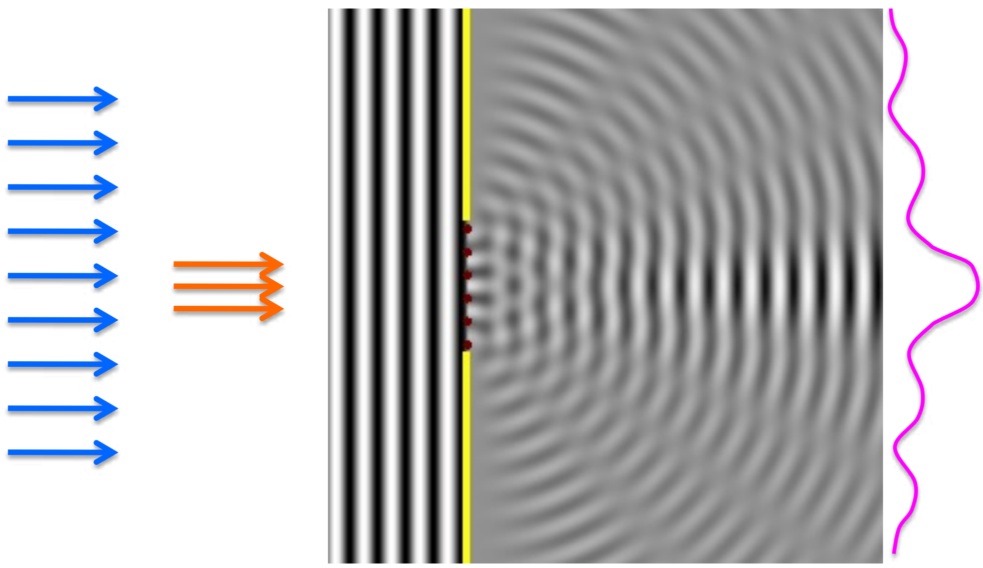

- Fresnel zone size > Phase modulator scale
  → Interference occurs
- Fresnel zone size < Phase modulator scale
  → Interference does not occur

Only small-scale structures create amplitude modulation.

Outflow speeds of solar corona derived from Akatsuki radio occultation scintillation data

Imamura et al. (2014, ApJ)

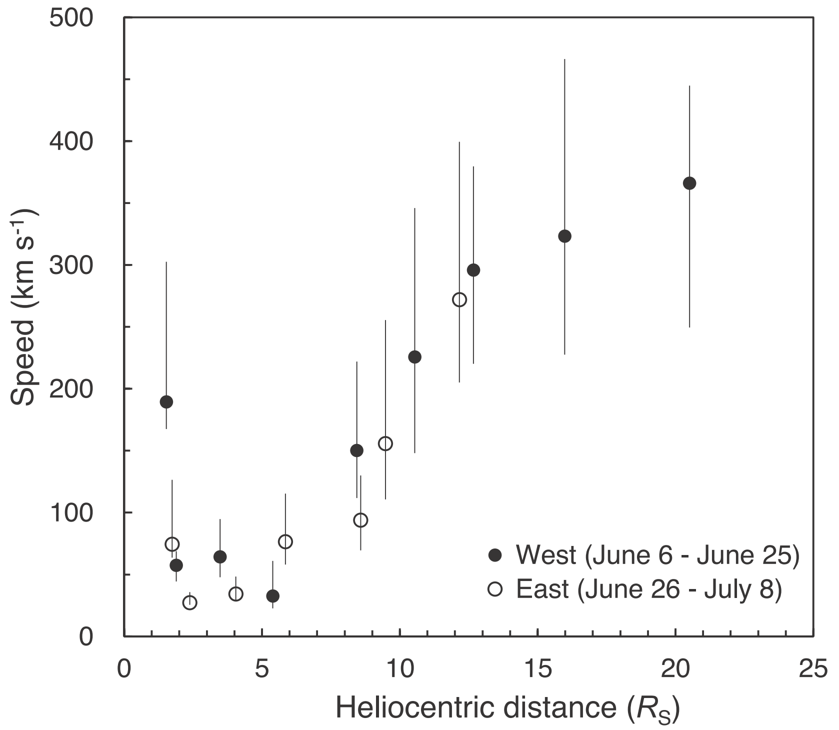

Microwave spectroscopy

ISS/SMILES for Earth’s stratosphere

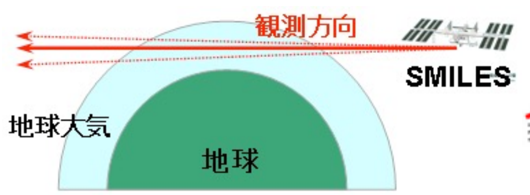

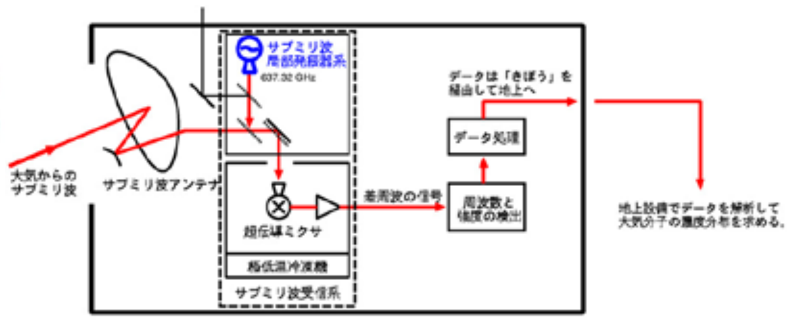

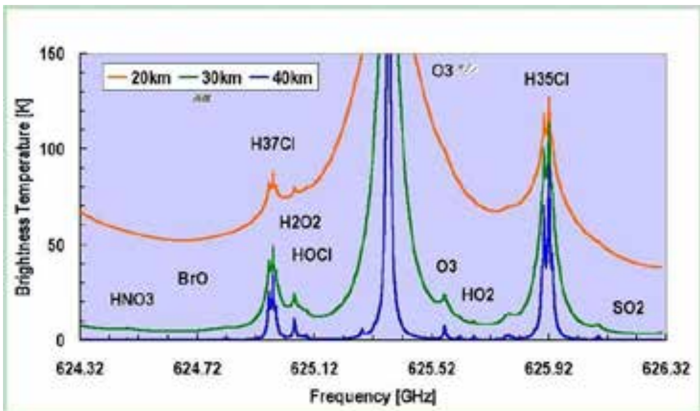

SMILES HP

ISS/SMILES for Earth's stratosphere

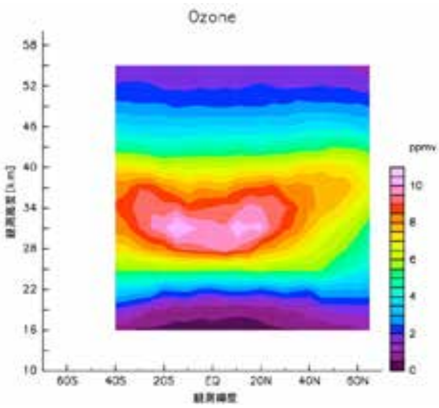

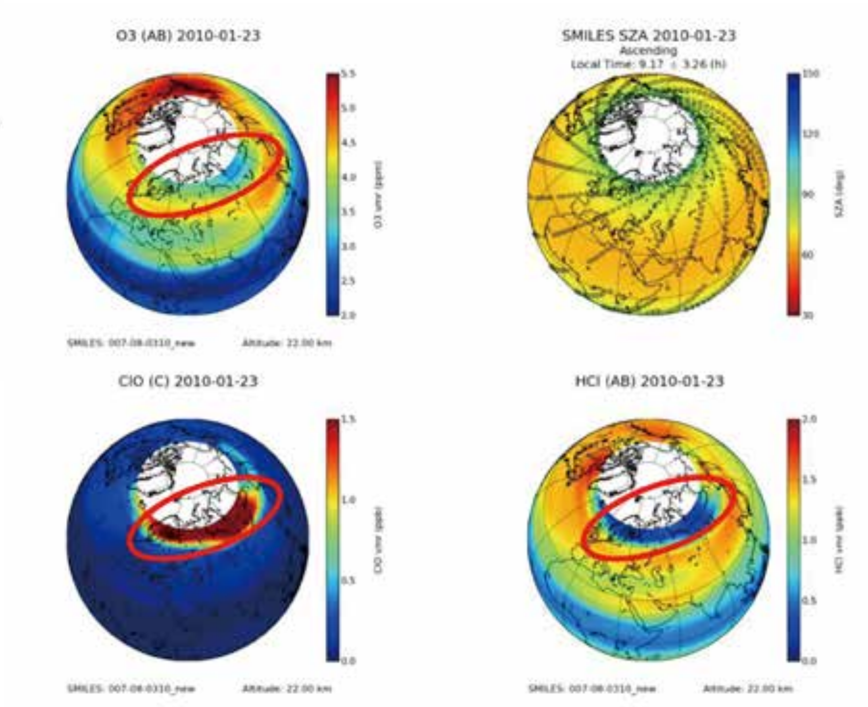

SMILES HP

JUICE(Jupiter Icy Moon Explorer)/ SWI(Submillimetre Wave Instrument)

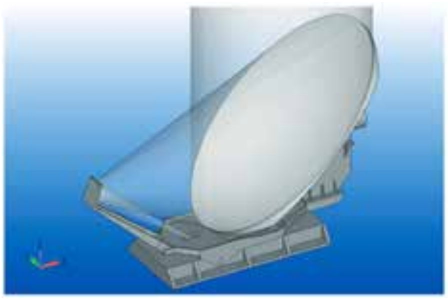

Kasai et al. (2014)

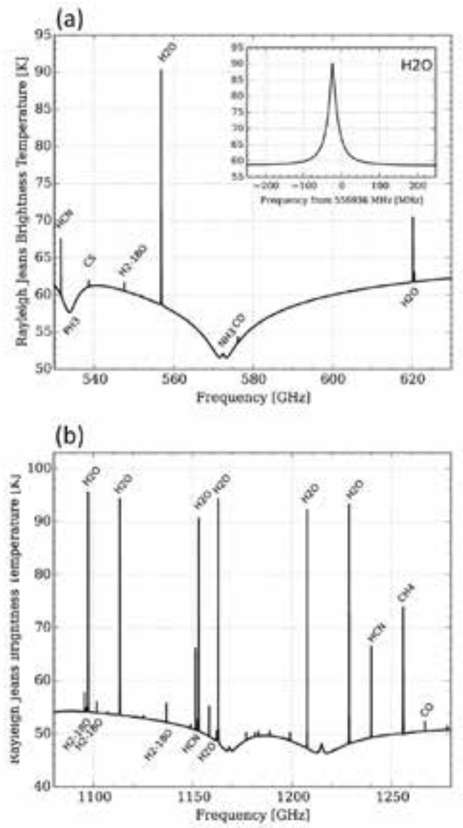

図1：SWIの観測周波数帯である(a)600 GHz帯および(b)1200 GHz帯における木星大気スペクトル(リム放射)のシミュレーション図．1000 hPaの接線高度を観測したケースを想定．(a)内部の図は，556 GHzのH_2O吸収線拡大図．木星大気の高速回転によって，吸収線の中心周波数がドップラーシフトをしている．

Microwave radiometer

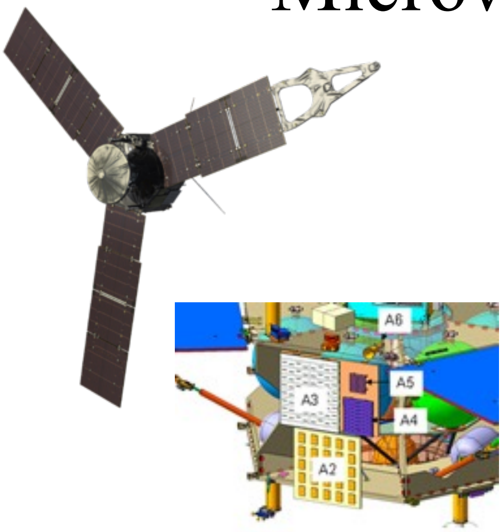

JUNO/MWR

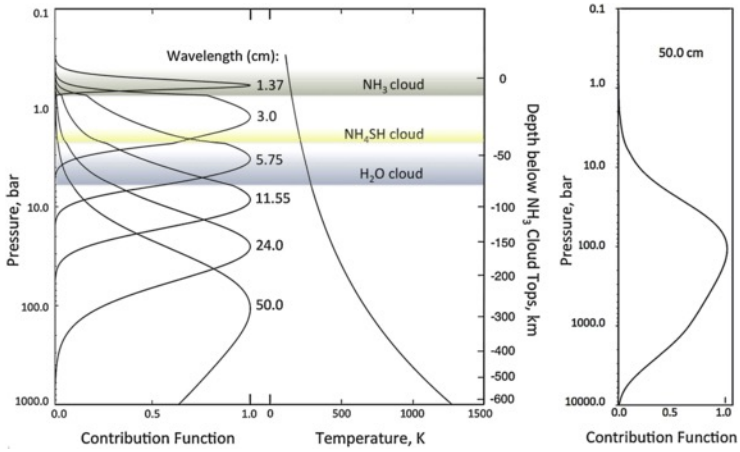

- measurements of electromagnetic waves on frequencies in the microwave range: 600 MHz, 1.2, 2.4, 4.8, 9.6 and 22 GHz, the only microwave frequencies which are able to pass through the thick Jovian atmosphere. Ammonia (NH_3) is the main opacity source.
- The radiometer will measure the abundance of water and ammonia in the deep layers of the atmosphere up to 200-bar (20 MPa; 2,900 psi) pressure or 500–600 km (310–370 mi) deep. The combination of different wavelengths and the emission angle should make it possible to obtain a temperature profile at various levels of the atmosphere.

Li et al. (2017)

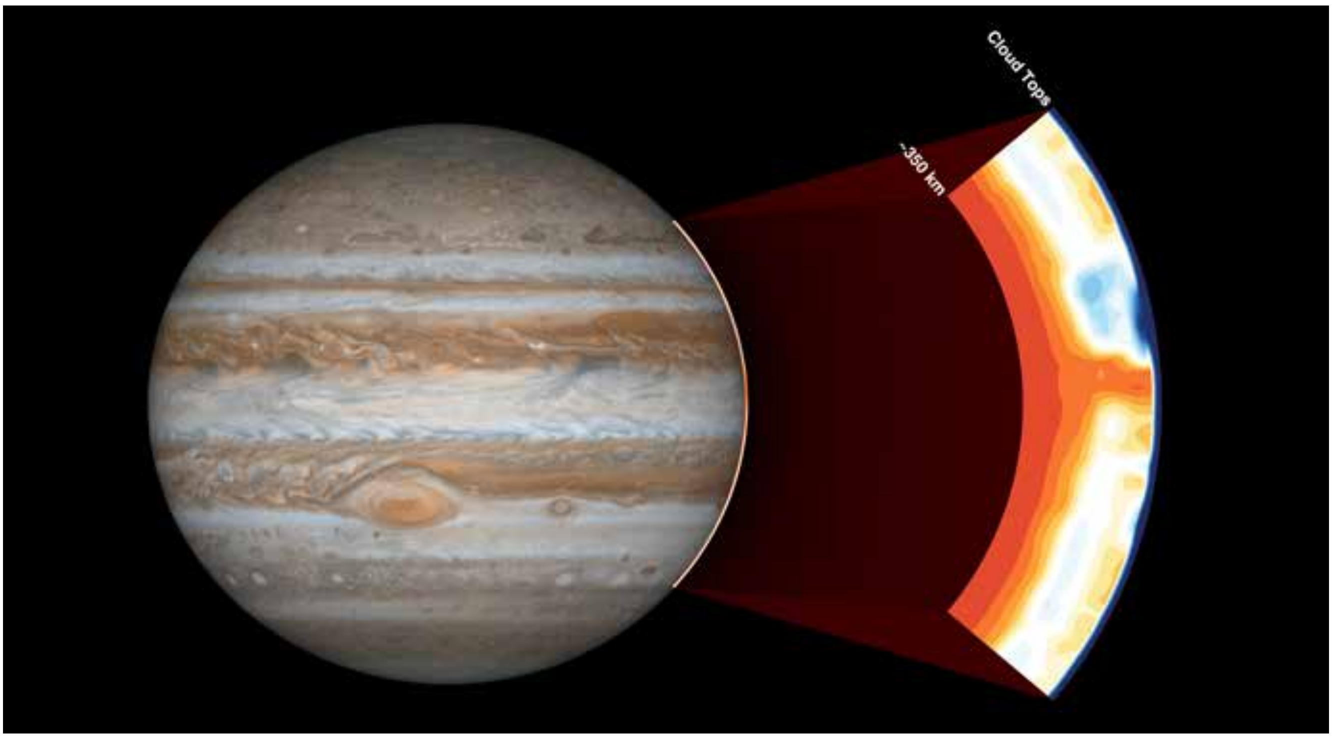

Figure 4. The colored contours show the ammonia concentration in parts per million inverted from nadir brightness temperatures during PJ1 flyby assuming that the deep water abundance is 0.06% (0.65 times solar). The deep ammonia abundance is 373 ppm, and the reference temperature is 132.1 K at 0.5 bar. The aspect ratio in the horizontal and vertical is exaggerated.

Doppler tracking of Juno spacecraft

- The spacecraft acts as a test particle falling in the gravity field of the planet. Jupiter’s gravity is inferred from range-rate measurements between a ground antenna and the spacecraft during perijove passes.
- The ground station transmits two carrier signals, at 7,153 MHz (X band) and 34,315 MHz (Ka band). On board, an X-band transponder and a Ka-band frequency translator lock the incoming carrier signals and retransmit them back to the ground station at 8,404 MHz and 32,088 MHz, respectively. The range-rate (Doppler) observable is obtained by comparing the transmitted and received frequencies.
- Spherical harmonics representation of planetary gravity fields is determined by the density distribution inside the body.

Doppler tracking of Juno spacecraft

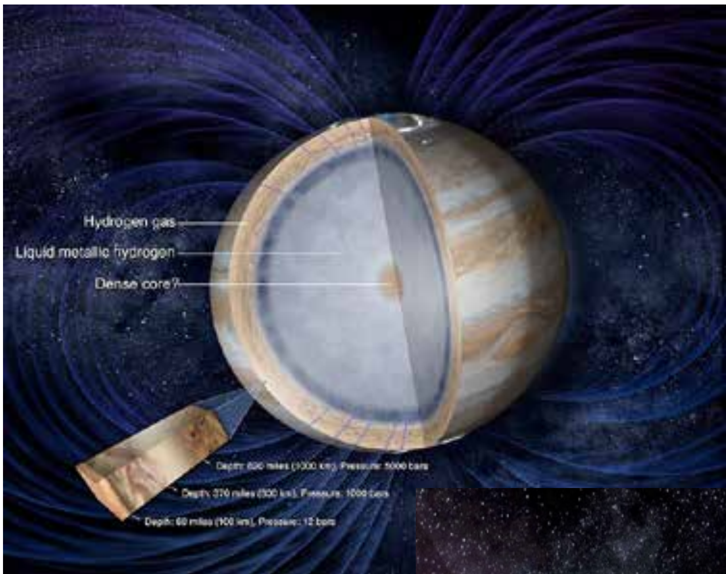

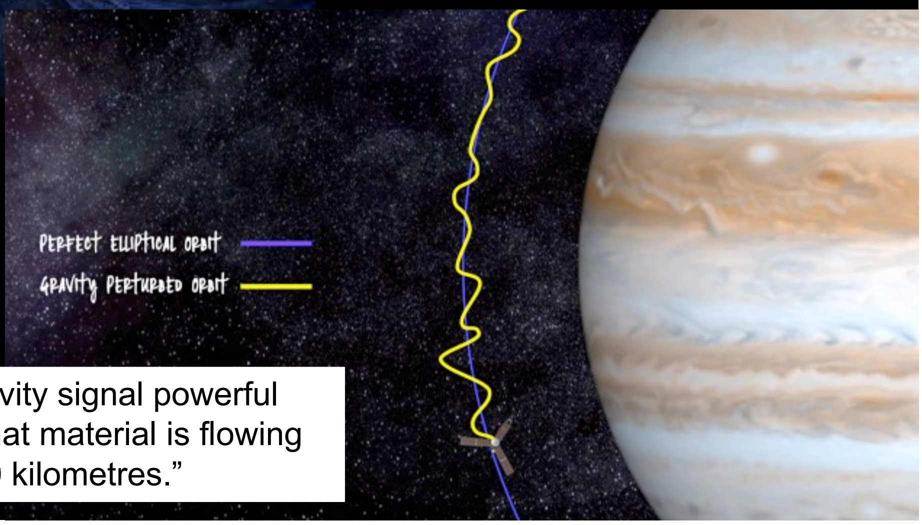

“Juno detected a gravity signal powerful enough to indicate that material is flowing as far down as 3,000 kilometres.”

Less et al. (2018)

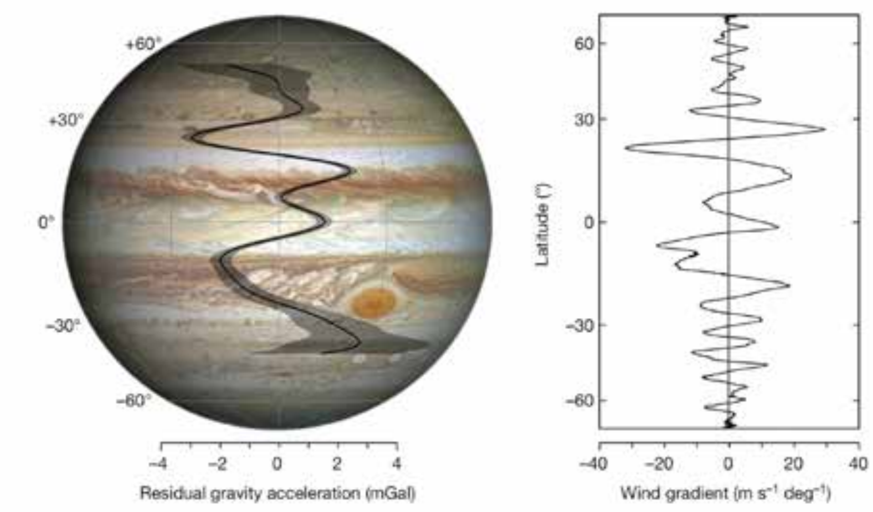

Figure 3 | Gravity disturbances due to atmospheric dynamics. a, An image of Jupiter taken by the Hubble Wide Field Camera in 2014 (https://en.wikipedia.org/wiki/Jupiter), showing the latitudinal dependence of residual gravity acceleration (in milligals, positive outwards) and associated 3σ uncertainty (shaded area) at a reference distance of 71,492 km, when the gravity from the even zonal harmonics J_2, J_4, J_6 and J_8 is removed. The residual gravity field, which is dominated by the dynamics of the flows, shows marked peaks correlated with the band structure. **b**, Latitudinal gradient of the measured wind profile. The largest (negative) peak of -3.4 ± 0.4 mGal (3σ) is found at a latitude of 24° N, where the latitudinal gradient of the wind speed reaches its largest value. The relation between the gravity disturbances and wind gradients is discussed in an accompanying paper[4].

“The observed jet streams, as they appear at the cloud level, extend down to depths of thousands of kilometres beneath the cloud level, probably to the region of magnetic dissipation at a depth of about 3,000 kilometres”